8-2016

Advanced Specialty Fiber Designs for High Power Fiber Lasers

Guancheng Gu
Clemson University

ADVANCED SPECIALTY FIBER DESIGNS FOR HIGH POWER FIBER LASERS

A Dissertation
Presented to
the Graduate School of
Clemson University

In Partial Fulfillment
of the Requirements for the Degree
Doctor of Philosophy
Photonic Science and Technology

---

by
Guancheng Gu
August 2016

Accepted by:
Dr. Liang Dong, Committee Chair
Dr. John Ballato
Dr. Eric Johnson
Dr. Lin Zhu

ABSTRACT

The output power of fiber lasers has increased rapidly over the last decade. There are two major limiting factors, namely nonlinear effects and transverse mode instability, prohibiting the power scaling capability of fiber lasers. The nonlinear effects, originating from high optical intensity, primarily limit the peak power scaling. The mode instability, on the other hand, arises from quantum-defect driven heating, causing undesired mode coupling once the power exceeds the threshold and degradation of beam quality. The mode instability has now become the bottleneck for average output power scaling of fiber lasers.

Mode area scaling is the most effective way to mitigate nonlinear effects. However, the use of large mode area may increase the tendency to support multiple modes in the core, resulting in lower mode instability threshold. Therefore, it is critical to maintain single mode operation in a large mode area fiber. Sufficient higher order mode suppression can lead to effective single-transverse-mode propagation.

In this dissertation, we explore the feasibility of using specialty fiber to construct high power fiber lasers with robust single-mode output. The first type of fiber discussed is the resonantly-enhanced leakage channel fiber. Coherent reflection at the fiber outer boundary can lead to additional confinement especially for highly leaky HOM, leading to lower HOM losses than what are predicted by conventional finite element mothod mode solver considering infinite cladding. In this work, we conducted careful measurements of HOM losses in two leakage channel fibers (LCF) with circular and rounded hexagonal boundary shapes respectively. Impact on HOM losses from coiling, fiber boundary shapes and coating indexes were studied in comparison to simulations. This work demonstrates

the limit of the simulation method commonly used in the large-mode-area fiber designs and the need for an improved approach. More importantly, this work also demonstrates that a deviation from circular fiber outer shape may be an effective method to mitigate HOM loss reduction from coherent reflection from fiber outer boundary.

In an all-solid photonic bandgap fiber, modes are only guided due to anti-resonance of cladding photonic crystal lattice. This provides strongly mode-dependent guidance, leading to very high differential mode losses, which is essential for lasing far from the gain peak and suppression of stimulated Raman scattering. We will show that all-solid photonic bandgap fibers with effective mode area of ~920μm^2 can be made with excellent higher order mode suppression. We then demonstrate a 50μm-core-diameter Yb-doped all-solid photonic bandgap fiber laser. 75W output power has been generated with a diffraction-limited beam and an efficiency of 70% relative to the launched pump power. We have also experimentally confirmed that a robust single-mode regime exists near the high frequency edge of the bandgap.

It is well known that incorporation of additional smaller cores in the cladding can be used to resonantly out-couple higher-order modes from a main core to suppress higher-order-mode propagation in the main core. Using a novel design with multiple coupled smaller cores in the cladding, we further scaled up the mode area and have successfully demonstrated a single-mode photonic bandgap fiber with record effective mode area of ~2650μm^2. Detailed numeric studies have been conducted for multiple cladding designs. For the optimal designs, the simulated minimum higher-order-mode losses are well over two orders of magnitudes higher than that of fundamental mode when expressed in dBs.

We have also experimentally validated one of the designs. M^2<1.08 across the transmission band was demonstrated.

Lowering quantum defect heating is another approach to mitigate mode instability. Highly-efficient high-power fiber lasers operating at wavelength below 1020nm are critical for tandem-pumping in >10kW fiber lasers to provide high pump brightness and low thermal loading. Using an ytterbium-doped-phosphosilicate double-clad leakage-channel fiber with ~50μm core and ~420μm cladding, we have achieved ~70% optical-to-optical efficiency at 1018nm. The much larger cladding than those in previous reports demonstrates the much lower required pump brightness, a key for efficient kW operation. The demonstrated 1018nm fiber laser has ASE suppression of ~41dB. This is higher than previous reports and further demonstrates the advantages of the fiber used. Limiting factors to efficiency are also systematically studied.

DEDICATION

This dissertation is dedicated to my family and friends,

for their love and camaraderie.

ACKNOWLEDGMENTS

First of all, I would like to extend my sincere gratitude and appreciation to my advisor, Dr. Liang Dong, for taking me on as his graduate student. Without his insightful advice, patient guidance, and continuous encouragement, my research would never have reached this far. I enjoyed the scientific enthusiasm and pursuit with him very much over the last five years. For me, he is not only my academic advisor, but also mentor for life.

I would also like to thank Dr. John Ballato, Dr. Eric Johnson, and Dr. Lin Zhu for taking their valuable time and being my committee member. I appreciate all of their advice and questions on my dissertation. I have taken courses from all of them during my graduate program and learned a great deal of knowledge.

To all my colleagues, Dr. Fanting Kong, Chris Dunn, Thomas Hawkins, Joshua Parsons, Maxwell Jones and Monica Kalichevsky-Dong, I am indebted to all of them for their effort and help. The completion of all these research projects are really the result of hard work and team collaboration of all of my group members. It is a pleasure and honor to work with all of them over the years.

Some special thanks to: Ying Yang and Yang Song for always inviting me for a big feast after a tired day; Yuan Li for all the time spent with you as a colleague and best friend; and Hua Tong and Leifeng Zhou for over a decade of friendships and being there for me through the best and worst time.

Finally, I am grateful for my family and my wife's unconditional support and love in every possible way. I will cherish those moments we spent together throughout my lifetime.

TABLE OF CONTENTS

Table of Contents (Continued)

Page

LIST OF TABLES

LIST OF FIGURES

List of Figures (Continued)

Figure

List of Figures (Continued)

Figure Page

LIST OF ACRONYMS

ASE—Amplified Spontaneous Emission

AS—All Solid

CCC—Chirally-Coupled-Core

CW—Continuous Wave

FEM—Finite Element Method

FM—Fundamental Mode

HOM—Higher Order Mode

LCF—Leakage Channel Fiber

LD-- Laser Diode

LMA—Large Mode Area

MCR—Multiple-Cladding-Resonance

TMI—Transvers Mode Instability

NA—Numeric Aperture

PBF—Photonic Bandgap Fiber

PCF—Photonic Crystal Fiber

RE-- Rare Earth

RI—Refractive Index

SBS—Stimulated Brillouin Scattering

SRS—Stimulated Raman Scattering

STRS—Stimulated Thermal Rayleigh Scattering

CHAPTER ONE

INTRODUCTION

1.1 High power fiber lasers and applications

In recent decades, fiber lasers have gained significant attention among a variety of industries. The advent of high power fiber laser has been a revolutionary force in many applications and quickly replaced other types of bulk lasers. The history of fiber lasers, in fact, is relatively brief. In early 1980s, optical fibers were mostly utilized as a waveguide for telecommunications [1,2]. Only limited research on fiber lasers and amplifiers was conducted during 1970s by a few pioneers such as Snitzer, Stone and Burrus [3–6]. The interest in using fiber as an active medium gained momentum in 1985 when Payne *et al* demonstrated first neodymium-doped fiber lasers [7,8]. The following of erbium-doped fiber amplifier operating in the third telecommunication window was rapidly adopted by the industry, leading to the wide spread of the internet [9]. Researches soon realized that fiber lasers possess a number of advantages comparing to its counterparts: 1) its unique geometry allows for stable single-transvers-mode propagation over a long distance; 2) high gains are allowed for very simple resonators and amplifiers as large single-pass gain can be achieved; 3) ease of splicing to other fibers permits realization of robust fiberized system without complicated free-space alignment, yielding minimum footprint; 4) large surface-to-volume ratio can facilitates heat extraction from the core, promising high average power operation. In addition to these intrinsic advantages, two other technologies, namely high power laser diodes (LD) and double-clad fibers, enable the power scaling to take off [10].

The schematic of cladding pumping is depicted in Fig. 1.1. It was firstly demonstrated in 1988 using a double-clad optical fiber whose core was doped with rare-earth (RE) element [11]. The principle of cladding-pumping is to turn the outer layer of coating to an outer cladding by coating the fiber with lower refractive index (RI) materials (usually polymers), so that the inner cladding that has higher RI becomes a pump core. The pump light from LD is directly launched into and confined within the pump core. The pump light then interacts with the active core along the propagation. Due to the large RI difference between fiber coatings and pump core, one can efficiently couple most of the pump power into the pump core with large acceptance angle, converting low brightness, multimode pump light into high brightness, single mode laser output.

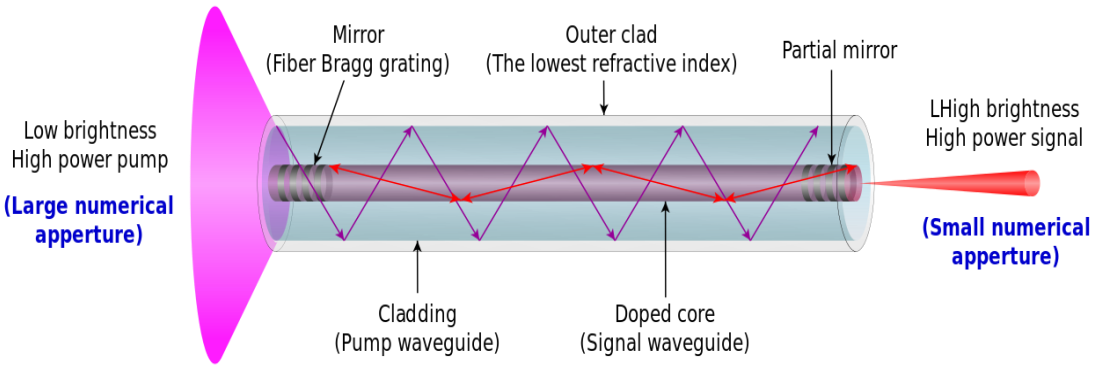

Fig. 1.1 Schematic of cladding pumping [12]

The advent of double-clad fibers and rapid deployment of high power LD triggered unprecedented power scaling of fiber lasers. During the last two decades of development, the average power output of a continuous-wave (CW) fiber laser with diffraction-limited beam quality has experienced exponential increase (see Fig. 1.2). It only took less than 25

years to scale up the average output power from less the l0W to 10kW [13–16]. The ultrashort-pulse fiber lasers also show similar power increase trend [17,18].

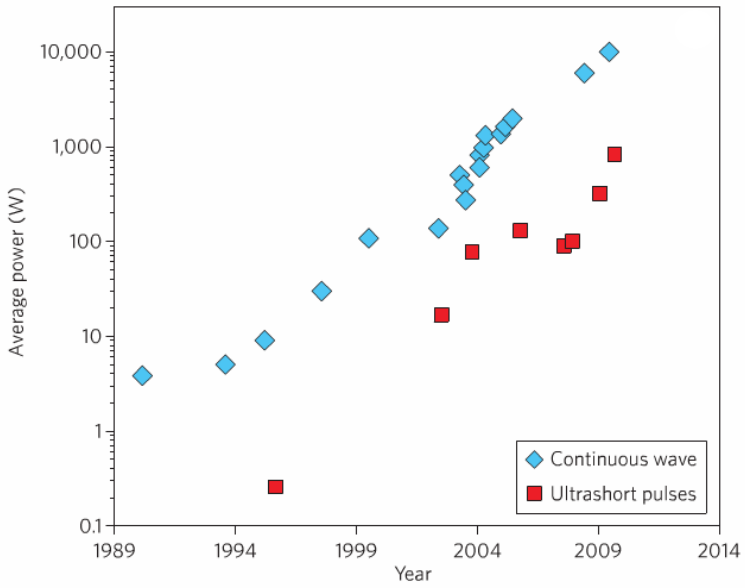

Fig. 1.2 Progress of high power diffraction limited fiber lasers [19].

Fiber lasers covers a wide spectrum of application scenarios in many industries. It is well known now that high power lasers can be used to machine a wide range of materials from plastics to glass and ceramics. Their non-contact nature makes them very low maintenance and cost-effective. An optical beam can be repositioned more rapidly than any mechanical tool, making it ideal for mass production. The machining precision with a diffraction-limited spot size is also significantly better than any conventional machining techniques. Another emerging applications is in defense. In 2015, a fiber-based laser weapon, the Navy's Laser Weapon System (LaWS) was deployed on the USS Ponce. The high output power can effectively destroy a target at much lower cost compared to

projectile weapons [20]. There are many academic applications as well. One of these is a laser-based particle accelerator, which promises to shrink current kilometer-long RF accelerators down to table-top ones [21]. High-order harmonics generation is another exciting application, promising to offer unsurpassed resolution for imaging and photo-lithography [22]. High-power single-frequency fiber lasers are critical for gravitational wave detection based on large-scale interferometers [23].

Fig. 1.3 The Laser Weapon System (LaWS) aboard USS Ponce [24].

1.2 Present limitations on power scaling

Despite the huge success of adoption of high power lasers. The demand for further power scaling is increasing. However, there are two main factors limiting the power scalability of fiber lasers, namely nonlinear effects and mode instability [25].

Nonlinear effects are as a result of high optical intensity in the core. The most detrimental nonlinear effects include stimulated Brillouin scatting (SBS), stimulated

Raman scattering (SRS), self-phase modulation and self-focusing [19]. The following section will offer a brief introduction for each of these nonlinear effects mentioned.

Stimulated Brillouin scattering (SBS)

SBS involves interaction between light and acoustic wave (usually caused by electrostriction) propagating in the fiber. A photon can be scattered into a photon with lower energy which usually propagates in the opposite direction, and an acoustic phonon [26]. The phenomenon is more pronounced when the bandwidth of the signal is narrow. This can prevent signal power from further increasing as the energy is constantly transferred from the signal light to back scattered light. Because of the nature of high power fiber lasers, it is very critical to increase the SBS threshold. Commonly used techniques include modulation of pump laser to broaden the laser linewidth or reduction of mode field overlap between light and acoustic mode by manipulating composition in the core [27].

Stimulated Raman scattering (SRS)

The stimulated Raman scattering involves interaction between light and molecular vibration of silica glass. Similar to SBS effect, a photon can be converted into another one with lower energy and an optical phonon. It can start from spontaneous Raman scattering or can be intentionally stimulated by seeding Stokes photons. But unlike SBS, SRS is a broadband effect and scattered light can propagate in forward and backward directions. Today, as the power levels reached beyond 10kW, SRS is the major bottleneck that limits the maximum output power of a fiber laser. Common mitigation techniques include use of

chirped-pulse-amplification or special fibers that can significantly attenuate the scattered beam [28].

Self-phase modulation

Self-phase modulation originates from the Kerr effect which describes the change of refractive index of the medium in response to an external electrical effect:

$$\Delta n = n_2 I \quad (1)$$

where n_2 is the nonlinear index component and I is the optical intensity. When the intensity of the light propagating in the fiber is high, the refractive index of the fiber is modified due to the Kerr effect. This will cause the variations in optical path and in turn modifies the phase of the light propagating in the fiber. This effect is particularly detrimental to ultra-short intense pulse laser since the Kerr effect will cause time-dependent phase shift corresponding to the temporal change of the pulse intensity [29]. For an un-chirped pulse, the SPM leads to spectral broadening even strong oscillation if SPM is strong enough.

Self-focusing

Self-focusing is the ultimate limit for power scaling. It is an extreme case of Kerr effect. It is induced by the change of RI due to very high intense light transmitting in the core. The fiber core with varied RI acts as a focusing lens which concentrates the light. As the beam radius decreases, the optical intensity becomes even higher, further enforcing the self-focusing effects. This self-enforcing process eventually collapses the beam into a very tiny spot and consequently destroy the fiber core [30]. Currently the peak power at which

self-focusing takes place is ~4-6MW at 1μm [31]. Self-focusing effect is difficult to circumvent and hence sets the ultimate ceiling for power scaling.

The nonlinear effects primarily limit the peak power scaling. In recently years, another limiting factor, transverse mode instability (TMI) has been observed in numerous literature reports that well behaved single-transverse-mode in a fiber laser can quickly deteriorates once the output power exceeds certain threshold [32–35]. When the output power is below the threshold, the fiber laser resumes the single-mode operation. It was soon discovered that the TMI is related to the thermal heating of the fiber lasers [33]. Nowadays, the TMI is widely considered to be stemmed from stimulated thermal Rayleigh scattering (STRS) [36]. In an active fiber, two propagating modes at slightly different frequencies will interfere with each other and form an intensity interference patter along the fiber. Due to the amplification, the quantum defect heating generates a travelling temperature wave that consequently changes the RI according to the modal interference [37]. The modulated RI profile essentially behaves like a grating, transferring energy from dominant fundamental mode (FM) to much weaker higher-order-mode (HOM) [36,38]. One might notice that this is also a self-enforcing process. The onset of TMI will severely degrade the mode quality and limit further increase of average output power.

1.3 Review on mitigation techniques on nonlinear effects and TMI

To date, the most effective way to mitigate the nonlinear effects is to increase the effective mode area [39]. The expansion of mode area will not only reduce the optical

intensity, but increase pump absorption and stored energy, leading to higher pulse energy in many pulse laser systems [40]. The main issue of mode area scaling is that the fiber will enter multimode regime as the core is enlarged, which will facilitate the mode coupling and worsen the TMI effect. Therefore, it is of primary importance to maintain single-mode quality in the large-mode-area (LMA) fiber.

Numerous approaches have been explored over the past decade (see Fig. 1.4). The first approach involves lowering numerical aperture (NA) while expanding core diameter so that single-mode operation can be preserved [41]. Recently, a number of low NA fibers have been reported with diameter ranging from 35μm to 52μm [42–44]. In particular, fibers with a NA of ~0.04 were used for 3kW demonstration [45,46]. One major deficiency of these approaches is that a lower NA weakens fundamental mode guidance and renders it very sensitive to bending and any other mechanical perturbation on the fibers [25]. Another type of specialty fiber, photonic crystal fiber (PCF) also falls into this category. A typical PCF consists of a solid silica-based central core and a lattice of periodically arranged air-hole cladding [47,48]. The lower effective NA significantly reduces the number of modes supported. The first photonic crystal fiber was proposed with a very small core size, which later inspired the development of large-mode-area photonic crystal fiber lasers [49–52]. Single-mode operation can be achieved by appropriately tailoring the air holes in the cladding. The high bending sensitivity due to the very low NA at large core sizes, however, makes a PCF only feasible to be used as a short stiff rod beyond 40μm core diameter, rendering it unsuitable for high average power lasers where longer fiber length is necessary for thermal management [53].

Apart from PCFs, other types of specialty fiber have also been proposed in order to increase the core size and minimize the HOM content. Some early approaches include resonant-ring designs and chirally-coupled-core (CCC) fibers [54,55]. Both rely on resonant out-coupling of higher order modes from a conventional step-index core while FM is well confined in the fiber core. They are, however, limited in terms of scaling much beyond 50μm core diameter. The higher order mode out-coupling fundamentally relies on phase-matching typically at a different wavelength for a different mode, and spatial overlap between the modes. However, both these aspects become major limits very quickly in a large core fiber. As such, it becomes difficult to ensure that all phase-matching conditions are met at the same desired wavelength for all relevant higher order modes when there are a number of modes in consideration, making these designs hard to implement, especially at large core diameters.

Some more recent approaches include leakage channel fibers [56,57]. They overcome the limitations of the resonantly-coupled approach by starting with a leaky waveguide. Because modes are no longer guided in a leaky waveguide, a significant new way for optimizing differential mode loss is possible. These highly leaky HOMs are no longer confined to the core and have, therefore, significant reduced overlap with active area of the fiber amplifier, minimizing the impact of quantum heating. Since these designs do not necessarily depend on any resonant effects or air-filling ratio, they are much more tolerant in the fabrication process compared to PCF and CCC. Due to the delocalized nature of modes, they are more scalable to much large core diameters. Robust single-mode operation with a flat-top mode in a Yb-doped LCF with ~50μm core was reported

recently [58]. The effective mode area was increased by 50% in a straight configuration for this core size, owing to the flat-top mode arising from by a slightly lower refractive index in the core center.

The last specialty fiber worth mentioning is the photonic bandgap fibers [59,60]. They usually have periodically arranged high-index rods embedded in the host materials forming the cladding. The core is created by omitting several high-index rods in the center. The PBF guides light based on the bandgap effect, meaning a mode is supported in the core only when it falls within the photonic bandgap of the cladding lattice. The light guidance only exists within a narrow spectral range, which can be used for lasing off the gain peak and SRS suppression [60,61]. A PBF can be designed to provide significant differential mode losses for FM and HOMs so that single-mode operation is possible for large core diameters. Theoretical and experimental studies have contributed to a large effective mode area of up to 900μm^2 previously [62–64].

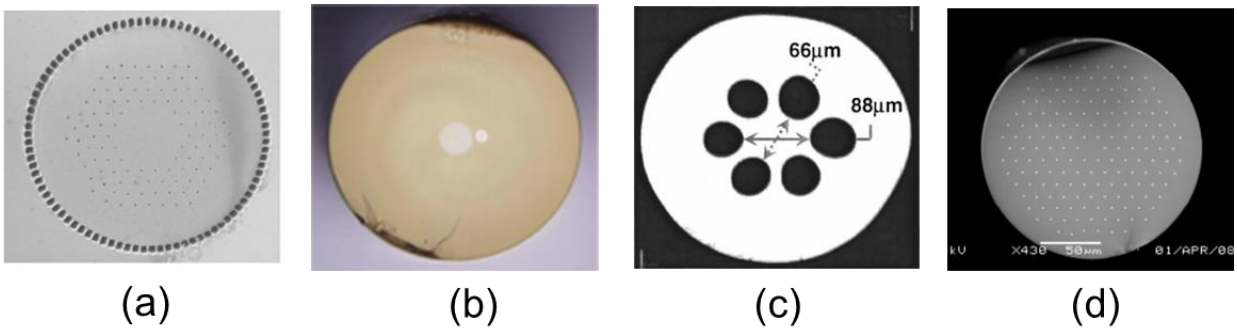

Fig. 1.4 Cross-section of specialty fiber designs: (a) photonic crystal fiber (PCF) [53]; (b) chirally-coupled-core fiber [55]; (c) leakage channel fiber [65]; (d) all-solid photonic bandgap fibers [40].

Four types of specialty fiber mentioned above are shown in Fig. 1.4. The comparison between these types of fibers are summarized in table. 1.1. Despite numerous specific techniques have studied for the suppression of a wide range of nonlinearities, the fundamental solution is to scale mode areas in fibers while maintaining sufficient single mode operation. Here the key problem is that more modes are supported once physical dimensions of waveguides are increased. The key to solve this problem is to look for fiber designs with significant higher order mode suppression. Seen from the table. 1.1, the all-solid LCF and PBF are the most two promising candidate for power scaling due to strong HOM suppression in the presence of LMA, good bend performance, and ease of fabrication and usage [66].

Table. 1.1 Comparison between PCF, CCC, LCF and PBF.

Fiber types	Bend performance	Fabrication complexity	Ease of use	Single-mode (D<50μm)	HOM suppression
PCF	Poor	Complicated	Poor	Excellent	Good for D<50μm
CCC	Good	Complicated	Good	Excellent	Good for D<50μm
LCF	Good	Easy	Good	Good	Strong
PBF	Good	Moderate	Good	Excellent	Strong

1.4 Dissertation outline

In this dissertation, the main focus will be on developing ytterbium-doped high power fiber lasers based on two types of specialty fiber, LCF and PBF. We will conduct detailed simulations and experimental studies on fiber's single-mode property and explore the fiber laser performance.

The dissertations will be organized as follow. Chapter 2 will discuss the new resonantly-enhanced leakage channel fiber (Re-LCF) with 50μm core diameter, which provides stronger HOM suppression compared to traditional LCF. We will demonstrate the limit of the simulation method commonly used in the large-mode-area fiber designs. The mode content measurement based on S^2 technique has found that deviation from circular fiber outer shape may be an effective method to mitigate HOM loss reduction from coherent reflection from fiber outer boundary.

Chapter 3 will be focused on AS-PBF with 50μm core diameter. More details about the guidance theory is offered in this chapter. Similar to Chapter 2, both simulation and experiment have been extensively conducted to characterize the effectiveness of single-mode operation. Both passive PBF and Yb-doped PBF are characterized for their HOM suppression and fiber laser performance. This work demonstrates the strong potential for mode area scaling of in single-mode all-solid photonic bandgap fibers.

Followed by Chapter 3, in Chapter 4, further mode area scaling of the PBF is explored. Several entirely new designs with resonant-coupling features are proposed

and simulated. Using a novel design with multiple coupled smaller cores in the cladding, we have successfully demonstrated a single-mode photonic bandgap fiber with a record effective mode area. For the optimal designs of a 100μm core fiber, the simulated minimum higher-order-mode losses are well over two orders of magnitudes higher than that of fundamental mode when expressed in dBs. We have also experimentally validated one of the designs.

From Chapter 2 to Chapter 4, the direction to reduce mode instability while increasing mode area is to minimize HOM content. Since the mode instability is driven by quantum defect heating, in Chapter 5, an ytterbium-doped fiber laser operating below 1020nm is constructed. By bring the laser wavelength closer to pumping wavelength, the quantum defect heating can be reduced by half, leading to significant reduction of TMI. Configuration of short wavelength fiber laser and experimental results are analyzed. Using an ytterbium-doped-phosphosilicate double-clad leakage-channel fiber with ~50μm core and ~420μm cladding, we have achieved ~70% optical-to-optical efficiency at 1018nm.

Finally, Chapter 6 will summarize the studies throughout the dissertation and outline the prospective research.

CHAPTER TWO

HIGH DIFFERENTIAL MODE LOSSES IN RESONANTLY-ENHANCED LEAKAGE CHANNEL FIBERS

2.1 Introduction

LCFs are particularly useful to generate high differential loss of modes. A typical geometric arrangement of LCF is shown in Fig. 2.1. It is worth noting that these LCFs are made entirely of glass without any air holes. The discontinuity of core-cladding boundary makes all modes leaky, allowing the fiber to be engineered to have high transmission loss for all HOM while maintaining negligible loss of FM [67]. Traditional LCF have identical cladding features placed periodically in the cladding, typically in a triangular matrix [65,68]. The features, however, do not have to be identical. In fact, both index and dimension of each cladding layers can be independently designed in order to cause resonance between the lowest-loss HOM and the 2D structured cladding. This resonance can pull the HOM further out into the cladding, leading to much improved HOM suppression of LCF. These LCFs are referred to as resonantly-enhanced leakage channel fibers (Re-LCF) [69]. Performance of Re-LCF with ~50μm core diameters was recently reported [69,70].

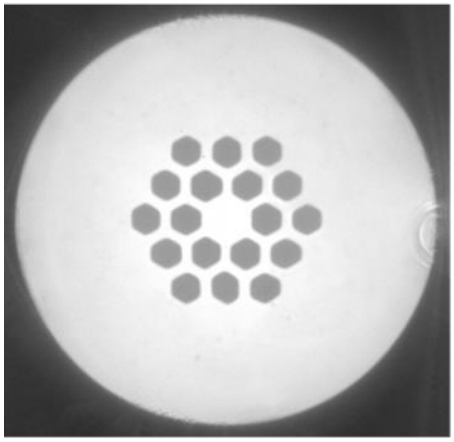

Fig. 2.1 Cross Section image of a typical LCF

Higher-order-mode losses are very important design parameters for the performance of fibers with large effective mode areas. They have, however, never been accurately measured in actual optical fibers. Using the S^2 technique, higher-order-mode content at the output of an optical fiber can be measured accurately [71]. This is typically done in a way that is hard to separate the contributions to higher-order-mode content at the output from many possible contributors such as launching conditions, fiber layout configurations, and fiber designs.

Design simulations are often based on the assumption of infinite cladding. This is a good assumption for well guided modes where light is mostly in the core. It is no longer a good assumption for highly leaky modes where a significant amount of light is radiated away from the core into the cladding. In this case, the reflection from any material interface, e.g. glass/coating boundary, in the fiber can provide additional confinement of the mode, leading to lower waveguide losses for the modes. The effect of circular glass/coating boundary on waveguide losses has been theoretically studied previously [56], showing that

the waveguide losses of modes are strongly dependent on the fiber diameter. This is not surprising, considering the coherent nature of the reflections.

Another important question is regarding the impact of refractive index of coating on the waveguide losses of modes. Double-clad fibers used in fiber lasers are often coated with a low-index polymer coating in order to provide a multimode pump guide [72]. Total internal reflection can take place at such boundary, completely trapping optical power in the guided modes of the highly multimode pump guide. The radiated power from modes guided mostly in the core region is expected to satisfy the total internal reflection condition at such boundary. Does this mean waveguide losses of core modes will vanish? It was speculated in [56] that the leaky core modes will still lose power to modes in the multimode pump waveguide in this case. This is, however, never proven.

For the further progress of mode area scaling of optical fibers, it is very important to accurately know the losses of higher-order modes in optical fibers and how they relate to designs. It is also very important to understand how factors such as coiling, fiber shapes and index of coating impact the waveguide losses in relation to designs. All these factors change the nature of reflection at material interfaces in fibers.

In an effort to answer some of these questions, we have accurately measured waveguide losses of modes using a cut-back technique in combination with a S^2 technique and a fully spliced configuration to ensure constant launch conditions. The measured waveguide losses were then compared to simulations based on infinite cladding. The test was conducted for a variety of coil diameters to identify any impact from coiling. Two Re-LCFs with ~50μm core diameter were tested. The first fiber has a circular glass/coating

boundary and is coated with standard coating with higher refractive index. The second fiber has a rounded hexagonal glass/coating boundary and is coated with low-index acrylic coating with a refractive index of 1.375.

2.2 Experimental characterization of Re-LCF

The cross-section images of the two fibers used in this work are shown in Fig. 2.2. The dimensions of features for each of the cladding layers are slightly different for optimized higher-order-mode losses at the operating coiling condition and around the wavelength of 1050nm. The fibers were designed to operate at a coil diameter of ~40cm, which is advantageous for applications requiring compact packing. For the circular Re-LCF, the core is 48μm at its smallest dimension (flat-to-flat) and 49.3μm at its largest dimension (corner-to-corner). The diameter of the circular Re-LCF is 392.7μm. For the hexagonal Re-LCF, the core is 50.9μm at its smallest dimension and 51.3μm at its largest dimension. The cladding is 426.1μm at its smallest dimension (flat-to-flat) and 449.3μm at its largest dimension (corner-to-corner). The two layers of features for both fibers is made from fluorine doped silica glass, whose refractive index is 0.0155 below silica. For the circular fiber Re-LCF, the average node size of inside layer is 30.1μm and outside layer is 28.31μm. For the hexagonal Re-LCF, the average node size of inside layer is 32.38μm and outside layer is 29.32μm. The circular Re-LCF is coated with a standard high index coating and was fabricated at Nufern. The hexagonal Re-LCF was drawn at Clemson with features fabricated at Nufern and is coated with low-index acrylic coating (n=1.375). This fiber was drawn at a slightly lower temperature in order to maintain the hexagonal shape of the stack.

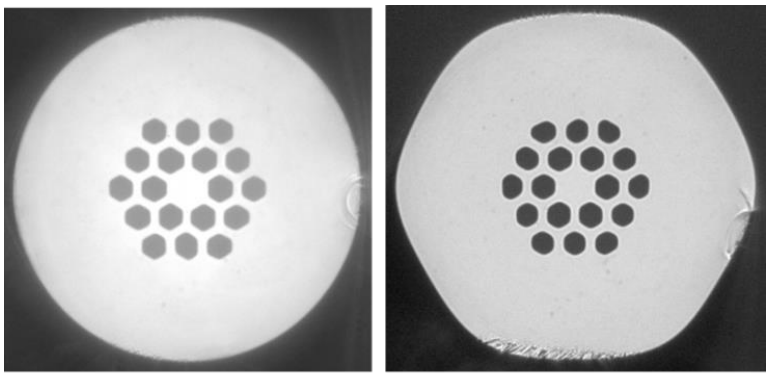

Fig. 2.2 Cross-section images of Re-LCFs used in this work, (a) circular Re-LCF and (b) hexagonal Re-LCF.

The feature boundaries were acquired from the cross-section images and were used in the simulations. We suppose the fiber is bent with a curvature radius R and the equivalent refractive index profile neq(x,y) is approximated as:

$$n_{eq}(x,y)=n_s(x,y)(1+x/R)$$

where $n_s(x,y)$ is the refractive index when fiber is straight [73]. A perfect matched layer (PML) is used to simulate the infinite cladding [74,75]. The simulation obtains complex effective refractive indices $n_{eff}=n_r+in_i$. The models used in the FEM mode solvers are shown in Fig. 2.2a and Fig. 2.2b for the circular and hexagonal Re-LCFs respectively. The loss is derived from the complex effective refractive indices:

$$Loss=20\times k\times n_i\times log_{10}(e)$$

where k is the free-space wavenumber.

In order to ensure launch stability during the measurements, the Re-LCF was spliced to a SM980nm fiber through a tapered mode adaptor to minimize the mode mismatch, which was fabricated by tapering the Re-LCF down to a core diameter of ~8μm

over a length of ~6cm. The S^2 technique was used to measure higher-order-mode content. It has a tunable laser and CCD for imaging capturing. The fiber was laid in a circular grove fabricated into an aluminum plate. The part of the fibers which was outside the circular grove is made to be as straight as possible. Circular groves with various diameters are fabricated into the same aluminum plate so that dependence on coil diameters can be tested.

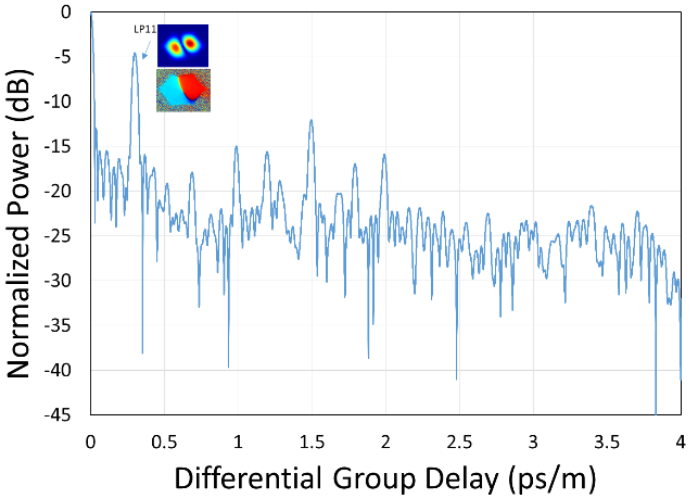

Fig. 2.3 Fourier transform of the spectrum versus differential group delay for circular LCF coil at diameter of 50cm. The insertion is the resolved LP11 mode pattern and phase.

Our S^2 setup has a ~-40dB detection limit in ratio of HOM power to FM power. In all of our experiments, only LP_{11} mode was observed in the two Re-LCFs. A sample of S^2 imaging is illustrated in Fig. 2.3. The sharp peaks followed by the LP_{11} mode are from multiple reflections from bulk optics in the system, which were carefully calibrated prior to the measurement. They can be easily identified due to their FM mode shape and always remain at the same location. The normal scan range was from 1026nm to 1076nm with a center wavelength of 1051nm. After power ratio of LP_{11} mode to LP_{01} modes was

determined at varying coil diameters, the fiber was cut by approximately 1m. The measurements were repeated for varying coil diameters. The fibers were cut back several times during the measurements. Eventually, in order to obtain HOM loss, the measured and normalized LP_{11} mode contents on a dB scale were plotted against the lengths of coiled fibers for each coil diameter and a straight line was fitted (see Fig. 2.4 for data at few selected coil diameters). Since the measured LP_{11} mode in the S^2 measurements always shows a well-defined narrow peak in delay, we have assumed that the coupling between LP_{01} and LP_{11} modes is minimal in our fibers. The fundamental mode loss is assumed to be negligible in arriving at the LP_{11} mode loss. This is largely true for the range of coil diameters used in the measurements. The slope of the straight line was regarded as the loss of the LP_{11} mode based on the two assumptions above. The error is estimated to be typically less than 10%. The FM loss was measured separately at fixed wavelength of 1050nm using a cut-back technique while ensuring fundamental mode at the output. The fiber lengths used in the experiment and related coil lengths at various coil diameters are summarized in Table 2.1 for the circular Re-LCF and hexagonal Re-LCF.

Table. 2.1 Fiber lengths of the circular Re-LCF used in the experiment.

Circular Re-LCF			Hexagonal Re-LCF		
Fiber length	Coil diameter	Coil length	Fiber length	Coil diameter	Coil length
9.8m	60cm	7.54m	7.8m	60cm	5.18m
	55cm	7.77m		55cm	5.18m
	50cm	7.85m			
	45cm	7.42m			
	40cm	7.85m			
	35cm	7.97m			
	30cm	8.71m			
9.0m	60cm	6.12m	6.6m	60cm	3.30m
	55cm	6.91m		55cm	3.45m
	50cm	6.28m			
	45cm	7.07m			
	40cm	7.54m			
	35cm	6.59m			
	30cm	7.54m			
8.2m	60cm	5.65m	5.8m	60cm	3.77m
	55cm	5.18m			
	50cm	6.28m			
	45cm	5.65m			
	40cm	7.54m			
	35cm	7.69m			
	30cm	7.54m			
7.3m	60cm	3.77m	4.9m	50cm	3.14m
	55cm	4.32m		45cm	2.12m
	50cm	4.71m		40cm	1.88m
	45cm	4.24m		35cm	1.65m
	40cm	5.02m			
	35cm	4.40m			
	30cm	6.59m			
6.4m	60cm	3.77m	4.0m	50cm	1.57m
	55cm	3.45m		40cm	1.57m
	50cm	3.14m		35cm	1.37m
	45cm	4.24m			
	40cm	3.77m			
	35cm	4.40m			
	30cm	5.65m			

5.3m	30cm	3.77m			
4.3m	30cm	2.83m			
3.3m	30cm	1.88m			

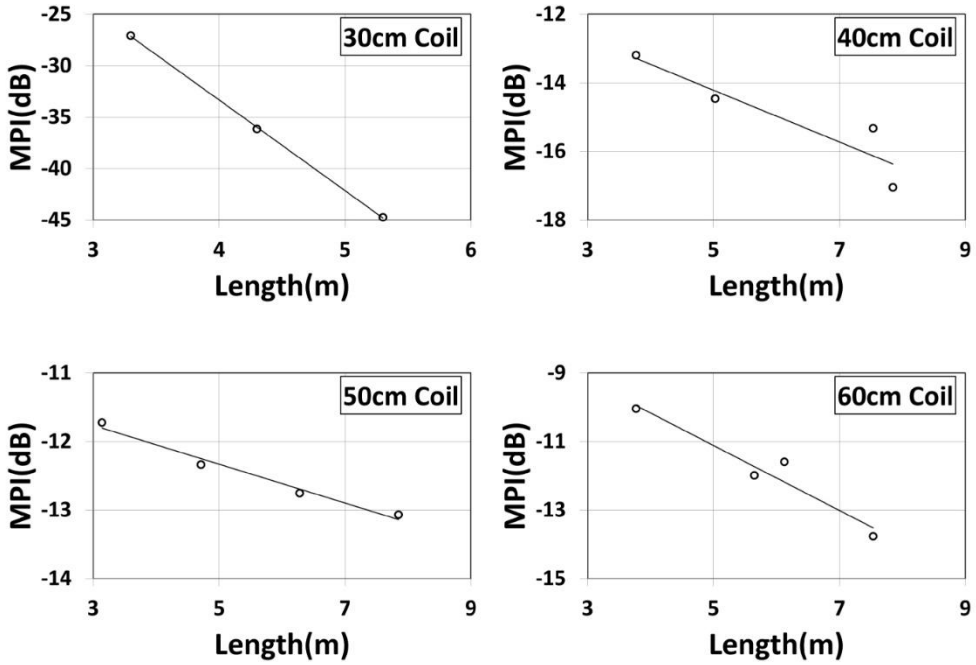

Fig. 2.4 Measured relative LP11 mode content (circles) versus coiled fiber length at various coil diameters for the circular Re-LCF and their linear fit (line).

The measured LP_{11} mode content, i.e. power ratio of LP_{11} and LP_{01} modes, is summarized in Fig. 2.5 for the circular Re-LCF. The coil lengths for each fiber length are different depending on coil diameters (see Table. 2.1). The LP_{11} mode content at the output is largely determined by the launch condition and LP_{11} mode loss over the coiled section of the fiber. The LP_{11} mode losses are determined, as described earlier, by the slope of linear fit to the measured LP_{11} mode content versus coil length data for each coil diameter. Due to the very high LP_{11} mode loss at 30cm coil diameter, much shorter fiber length had to be used in this case (see Fig. 2.5).

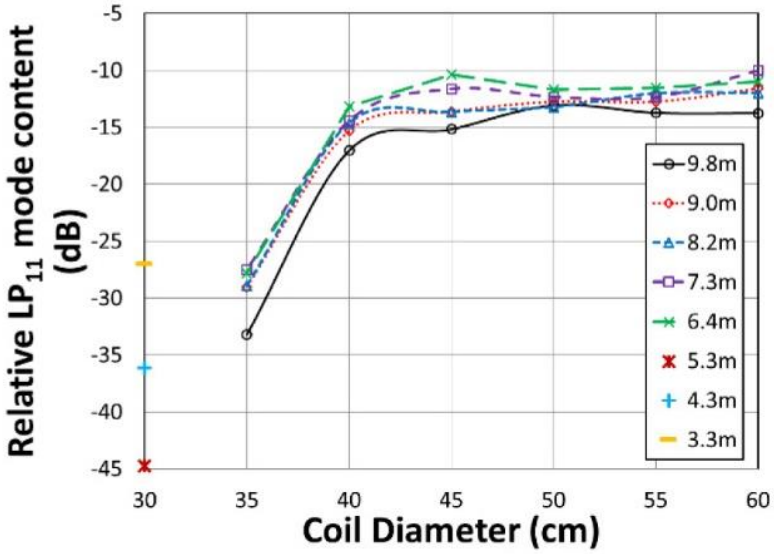

Fig. 2.5 Measured relative LP11 mode content at various coil diameters for the circular Re-LCF.

2.3 Impact of fiber outer boundaries on leaky mode losses

The simulated loss for the fundamental mode, second mode and third mode are shown in Fig. 2.6. The second mode and third mode are two different orientations of the LP_{11} mode (see insets in Fig. 2.6). The measured FM loss is also shown along with the measured LP_{11} mode loss. Two sets of FM measurement are shown, one with free space launch and one with spliced input. The fiber was designed for operation at a coil diameter of 40cm. At smaller coil diameters, the predicted FM loss can be very high (see Fig. 2.6 for diameters less than 0.35m). As it can be seen, the measured FM losses fit well with the simulation in the low loss regime. This is consistent with what we expected. The mode is well confined to the core region in the low loss regime. There is very little impact from

what is going on far beyond the core. The measured FM losses are, however, lower than the simulation in the high loss regime when coil diameter is below 35cm.

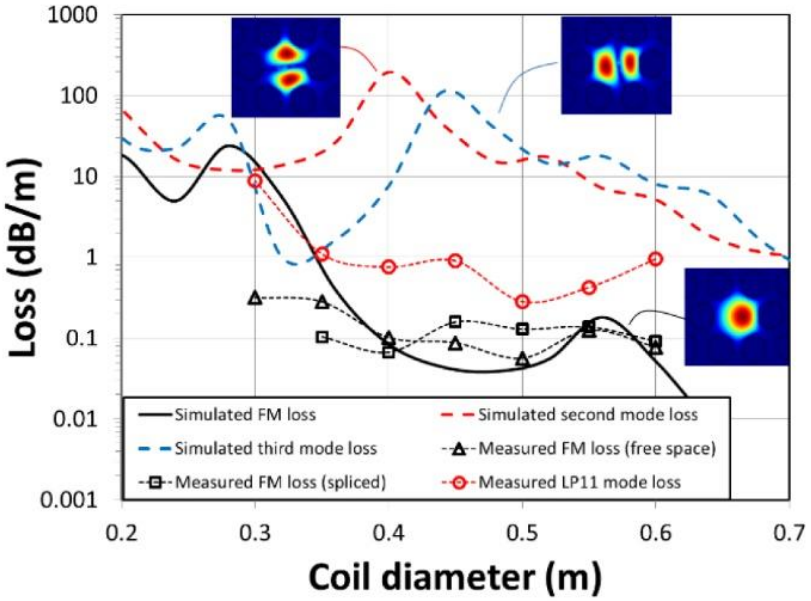

Fig. 2.6 Simulated and measured mode losses in the circular Re-LCF.

The measured LP_{11} mode losses are, however, much lower than the simulation at large coil diameters. The difference between the measured LP_{11} mode losses and the simulation, however, converges at small coil diameters when coil diameter is below 0.35m. The lower measured losses of both the fundamental and LP_{11} modes in the predicted high loss regime can be explained by the reflection at the circular glass/coating boundary. The modes which are significantly radiated away from the core into the cladding are likely to be reflected back to the core due to the coherent reflection, leading to much lower waveguide loss than the simulated. The LP_{11} mode is designed to have high waveguide loss and consequently, is expected to experience larger impact from the coherent reflection at the fiber glass/coating boundary. The convergence of the measured LP_{11} mode losses and

the simulation at smaller coil diameters is interesting. This may be an indication that phase walk-off in the reflection from the curved cylindrical boundary of the coiled fiber can mitigate the coherent reflection at small coil diameters. It is worth noting that, since we could not distinguish the LP_{11} mode with the two different orientations illustrated in the insets in Fig. 2.6, our measured data represent an average of the two orientations. Our tunable light was slightly polarized and there was no polarization control in the measurement.

To investigate further on how to mitigate the effect of the coherent reflection from fiber boundary, we conducted the same set of measurements on the hexagonal Re-LCF. This fiber is coated with low-index polymer coating (n = 1.375) to simulate the effect of double-clad fiber. In a double-clad fiber, optical powers can be trapped within the pump guide due to the total internal reflection at the interface between pump core and cladding, leading to potentially lower HOM losses than those with high index coating. Since this is the situation where most large mode area fibers are used, it is very important to understand the impact of pump cladding on the HOM losses in this case. The simulated mode losses for the fundamental mode, second mode and the third mode for this fiber are shown in Fig. 2.7. The simulation present similar loss pattern as those in Fig. 2.6. The minor differences of the loss curves between the circular and hexagonal Re-LCF are mainly caused by slightly different dimensions of the features. This fiber was also designed for operating at ~40cm coil diameter. The measured mode losses are also shown in the figure. It is interesting to see the LP_{11} mode losses fit reasonably well with the simulation even at large coil diameters. This is a dramatic improvement on HOM losses compared with those in the

circular LCF. Since the radiated optical powers from the core modes are expected to be trapped by the pump cladding it is reasonable to assume that the loss of LP_{11} mode power is through reflection into modes of the multimode pump guide at the pump core and cladding interface [56]. The result is a strong indication that non-circular pump cladding can be very effective in mitigation of the coherent reflection at the pump core and cladding interface. This is significant and confirms the validity of the design approach based on suppression of HOM propagation for mode area scaling. The measured FM losses also fit reasonably well to the simulation (see Fig. 2.7).

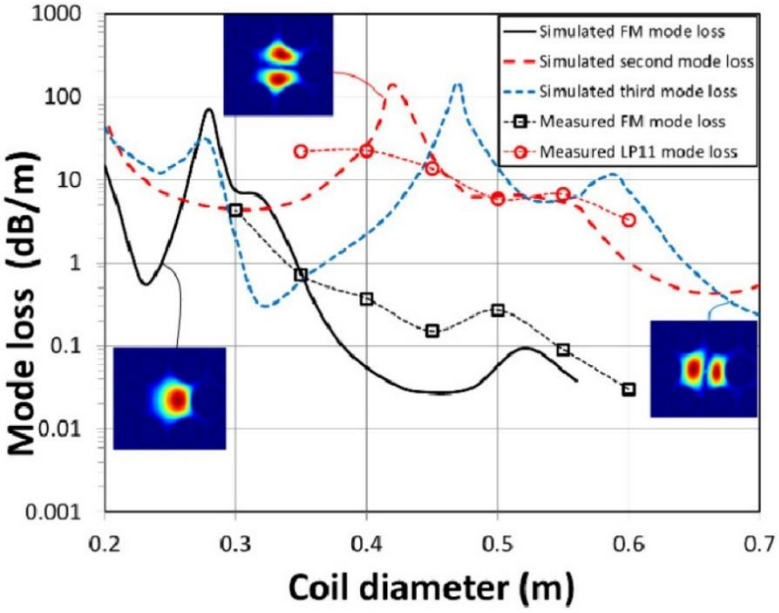

Fig. 2.7 Simulated and measured mode loss in the hexagonal Re-LCF.

Effective mode area of FM was also simulated for the hexagonal Re-LCF for various coil diameters in Fig. 2.8. The effective mode area is ~900μm^2 at the operating coil diameter of 40cm.

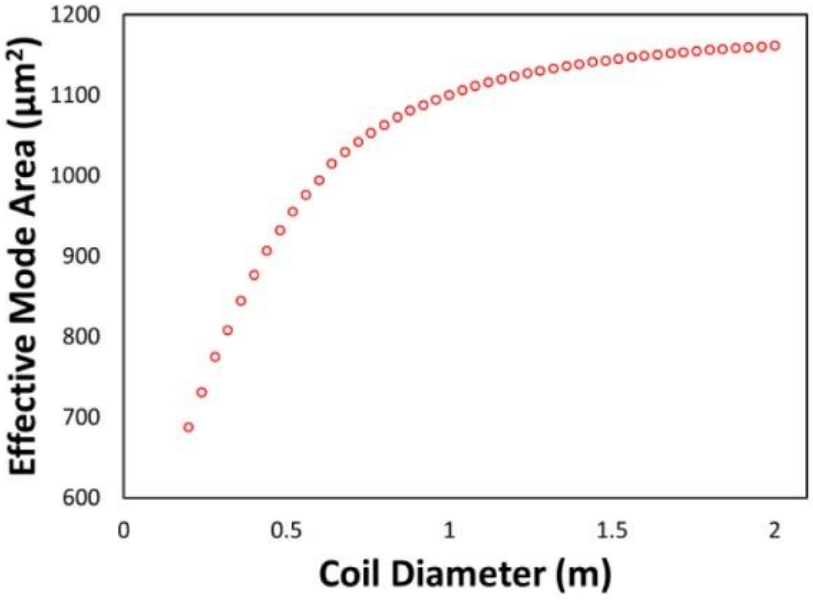

Fig. 2.8 Simulated effective mode area in the hexagonal Re-LCF.

The wavelength dependence of LP_{11} mode content can be measured by dividing the wavelength scan used in the S^2 measurement into a number of smaller sub-scans with equal wavelength span. This was done in Fig. 2.9 for the LP_{11} mode content in the 4m hexagonal Re-LCF coiled in 35cm diameter coil. The sub-scan has a wavelength range of 10nm. Wavelengths at the center of each sub-scan are used for the plot. The flat wavelength dependence over this wavelength range is expected and consistent with the simulation. It is worth noting that ~-40dB HOM suppression can be achieved over such a short fiber length, especially considering the short length of the coiled section of ~1.4m (see Table. 2.1).

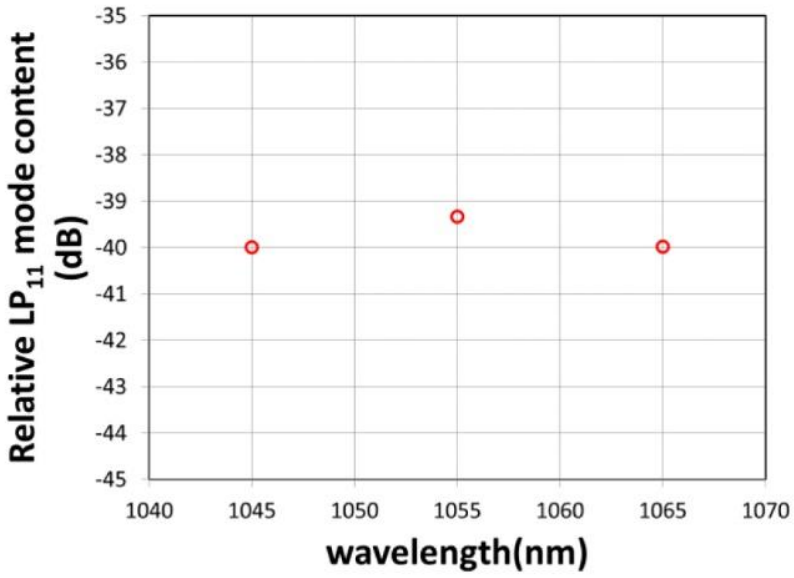

Fig. 2.9 Wavelength dependence of the measured LP11 mode content in the 4m hexagonal Re-LCF in 35cm coil. Coiled length is 1.37m.

Differential group delay between the LP_{01} and LP_{11} modes can also be measured by dividing the total wavelength scan in the S^2 measurement into a number of sub-scans of equal wavelength span. The differential group delays were obtained from the S^2 measurement of the circular Re-LCF and are plotted against the center wavelengths of each of the sub-scans in Fig. 2.10. The differential group delay was also simulated by a multipole mode solver using approximate circular features and is also plotted in Fig. 2.10. There is an excellent agreement between the measured differential GVD and the simulation. Same results were also observed on hexagonal Re-LCF.

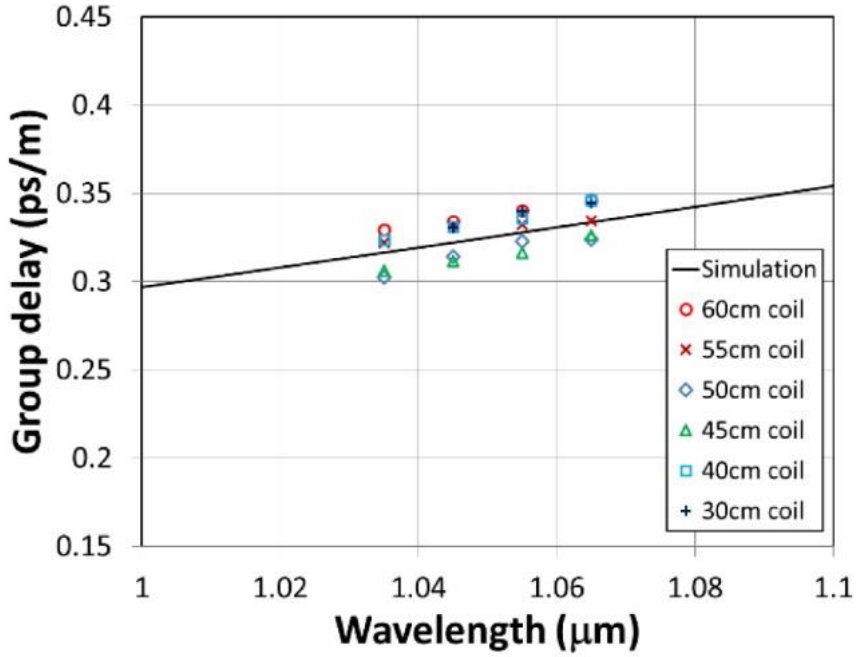

Fig. 2.10 Simulated and measured differential group delay between LP01 and LP11 modes in the circular Re-LCF. The simulation was done for a straight fiber. The measurements were performed at a range of coil diameters.

2.4 Conclusion

In this work, we conducted careful measurements of HOM losses using a cut-back technique in combination with a S^2 technique and a fully spliced configuration to ensure launch stability. Impact on HOM losses from coiling, fiber shapes and coating indexes were studied in comparison to simulations based on infinite cladding.

The results confirm that the simulation based on infinite cladding is accurate for well confined modes with low waveguide losses. But for the highly leaky modes, the measured losses can be significantly lower than what are predicted by conventional simulation method at large coil diameters in the circular LCF. The measured loss, however,

start to approach the simulation results at smaller coil diameters. The measured losses of the highly leak modes in the hexagonal LCF, on the other hand, are consistent with the simulation even at large coil diameters.

The results show that tight coiling can mitigate the effect of coherent reflection at outer boundary in fibers, possibly due to phase walk-off from the coiled cylindrical surface. The results from the rounded hexagonal fiber are even more startling. HOM losses in excess of 20dB/m were measured in the hexagonal Re-LCF with ~50μm core diameter. It suggests that a deviation from circular boundary can be very effective in mitigating the impact of the coherent reflection from outer boundary in fibers. The low-index polymer coating on this fiber does not seem to matter at all. This is strong evidence that the radiated powers from the core are reflected into the guided modes in the multimode pump waveguide. This is also a strong proof that the design concept of exploiting strong leakage losses of HOMs works even in double-clad fibers with a suitable design of fiber boundary.

CHAPTER THREE

YTTERBIUM-DOPED LARGE-MODE-AREA ALL-SOLID PHOTONIC BANDGAP FIBER LASERS

3.1 Introduction

The all-solid PBFs have been viewed as a promising candidate for realizing high power fiber lasers and amplifiers because of its best HOM suppression capability for the same effective mode area [59,60]. This is due to a combination of three key factors. They have an open cladding which provides a leaky waveguide where mode-dependent losses can be introduced. The cladding is highly dispersive as one would expect in a photonic bandgap cladding, enabling designs which can also provide mode-dependent guidance. Lastly, the cladding effective index changes significantly within the bandgap due to the highly dispersive cladding, enabling a single-mode regime near the high-frequency end of the bandgap [76].

In all-solid photonic bandgap fibers, a mode is guided only when it falls within the photonic bandgap of the cladding lattice. This provides great potential for creating designs that support only the fundamental mode, i.e. selective mode guidance versus selective elimination of mode guidance as in some other approaches. The robust optical guidance and physical constructs of all-solid PBFs enable them to be made and used much like conventional fibers. Double-clad designs and polarization-maintaining can be added with ease [77]. Transmission can be made with strong wavelength-dependence in these fibers

for use in SRS suppression, accomplished by introducing strong loss at the Raman Stoke wavelength, in FWM suppression by providing appropriate dispersion, and in lasers at wavelengths normally dominated by much stronger transitions [60].

Mode area scaling to 20μm mode field diameter using all-solid photonic bandgap fibers was reported few years ago [78]. A detailed theoretical investigation on the limit of mode area scaling with all-solid photonic bandgap fibers was reported recently, indicating an upper limit of ~500μm^2 using a more optimized seven-cell core and operating in the first bandgap [79]. Recently, all-solid photonic bandgap fibers with up to ~700μm^2 effective mode areas have been demonstrated operating in the first bandgap [60,64].

In this chapter, we will start with the brief discussion on the guidance theory of AS-PBF. we will report both theoretical and experimental studies of mode-area-scaling with all-solid photonic bandgap fibers to beyond 900μm^2 which has the capability to delivery 30 times of power as regular single-mode fiber without reaching the non-linear threshold. The quantitative mode content measurements show that excellent single mode output can be obtained from theses fibers in length scale close to what is required for fiber laser and amplifiers. We will also demonstrate an Yb-doped all-solid photonic bandgap fiber laser with a core diameter of ~50μm. The calculated effective mode area is ~1450μm^2 in a straight fiber, which is over a factor of 4 increase over that previously demonstrated in a ytterbium-doped all-solid PBF [60]. We have also tested the laser performance and beam quality. Strong single-mode propagation was observed.

3.2 Guidance theory of AS-PBF

Guidance properties of all-solid photonic bandgap fibers and their fairly matured fabrication processes are well understood [80–84]. These fibers have a background glass and a cladding lattice of high index nodes (Fig. 3.1a). The cladding is defined by node diameter d, pitch Λ, node index n_h and background index n_b. The photonic bandgap effect of the cladding lattice, i.e. anti-resonant effects of the cladding lattice, guides light in the core of the fiber. The bandgaps in the cladding is illustrated as the white areas in Fig. 3.1b. The horizontal axis in Fig. 3.1b is the normalized frequency of the node, $V/\pi = (d/\lambda)(n_h^2 - n_b^2)^{1/2}$ and the vertical axis modal index minus n_b. The guided modes in the defect core only exist within the cladding bandgaps, which determine the wavelength range over which the modes in the core are guided. This photonic bandgap guidance can be strongly mode-dependent. A large core all-solid PBF can potentially be designed by maximizing guidance of the fundamental mode while minimizing the guidance of all higher order modes, equivalent to the use of mode-dependent leakage losses. As in conventional fibers, the effective indices of the core modes are just slightly below the core index n_b. First three modes in the first bandgap of an all-solid photonic bandgap fiber with 50μm core are illustrated in Fig. 3.2, showing strong guidance of fundamental mode and weakly guided higher order modes.

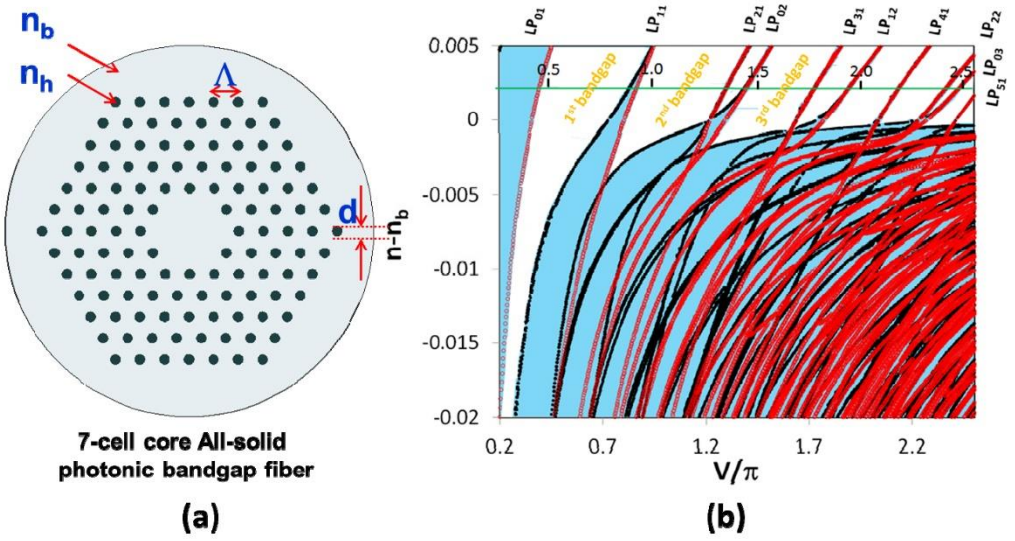

Fig. 3.1 (a) Illustrations and parameter definitions of a seven-cell-core all-solid photonic bandgap fiber, and (b) photonic bandgaps of the cladding lattice (Δ = 2.07%).

The first all-solid photonic bandgap fiber was demonstrated in 2004 [85]. The refractive index of the nodes in the cladding was ~16% above that of the background glass. The nodes were made of SF6 with an index of ~1.79 and the background glass was made of LLF1 with an index of 1.54. In the next demonstration in 2005, the refractive index of the nodes in the cladding was just 1% above the silica background [82]. High index contrast had been considered to be a key to photonic bandgaps. This was the first demonstration that guidance based on photonic bandgaps in optical fibers can take place at arbitrarily weak refractive index contrast. This is fundamentally due to the fact that the guided modes in the defect core are impinging on the photonic bandgap cladding at a very shallow glancing angle. The bandgap only needs to exist for such a small glancing angle, which significantly relaxes the requirement for high refractive index contrast. The multiple bandgaps are easily observed in these early fibers.

The next significant breakthrough was the thorough understanding of the origins of the photonic bandgaps in the cladding by Birks *et al*. [81] The key is to understand the modes supported by the photonic bandgap cladding. Due to the periodic nature of the cladding, these modes are not the localized modes we typically see in waveguides, but these global modes have their origin in the localized modes supported by each individual node. In a photonic bandgap cladding, they form bands of global modes, see Fig. 3.1b. Each band can be traced back to the localized modes guided in the nodes which are labeled in Fig. 3.1b. The definitions of relevant fiber parameters are given in Fig. 3.1a, where Λ is the spacing of the cladding nodes; d is the node diameter, n_b is the background glass index and n_h is the node index. The transverse electric field of the mode at the upper edge of the first band, labeled LP_{01} in Fig. 3.1b, is shown in Fig. 3.2a and that at the lower edge of the first band is shown in Fig. 3.2b. These global modes in the bands can be viewed as arising from the localized mode coupled to its nearest neighbors. Since the phase of the field over neighboring nodes can take an infinite number of combinations, there are an infinite number of global modes within each band at any specific frequency, in an infinite cladding. The top of the band is from modes with equal phase over neighboring nodes, see Fig. 3.2a. The bottom of each band is from modes with anti-phase over neighboring nodes, see Fig. 3.2b. It was realized very quickly that the even-order bandgaps are shallower than the adjacent odd-number bandgaps in refractive index due to the difference in the field distributions of the global modes which form the bandgaps [81]. For even-order bandgaps, the relevant global modes are more concentrated in the low-index background.

A recent theoretical work has determined that a seven-cell all-solid photonic bandgap fiber can achieve an effective area of 511μm^2 in a fiber with a core diameter of ~42.2μm when operating in the first photonic bandgap at ~1μm and being coiled at radius R = 10cm [79]. Further mode area scaling is limited by significant increase of fundamental mode loss at large pitch required for larger cores, noting core diameter $2\rho = 4\Lambda - d$ for a seven-cell core. Higher order bandgaps are usually associated with shallower bandgaps and, consequently, high losses (Fig. 3.1b). However, this loss can be significantly lowered by an increase of d/Λ. Operating in the third bandgap allows choosing a much larger d/Λ, by almost a factor of three. This is more than what is required to compensate the loss caused by the reduced bandgap depth, leading to an overall lower loss for the fundamental mode and, consequently, much larger core diameters for using the third bandgap. In this work, we will demonstrate further mode area scaling is still possible with the operating in the third bandgap.

3.3 Mode are scaling of AS-PBF with core diameter of 50μm

An AS-PBF with core diameter of 50μm was fabricated using standard stack and draw procedures. The nodes in the cladding are made from a graded index MM preform with germanium doped core with peak $\Delta = 1.72\%$. The fiber has core diameters of 55.1μm. The flat-to-flat dimension and corner-to-corner dimension of the cladding are 373μm and 411μm, respectively. The node diameter is 15.3μm and pitch distance is 6.1μm The cross sections of the two fibers are shown in Fig. 3.2. Effective mode area is simulated at various coiling diameters and is shown in Fig. 3.3, showing an effective area of ~900μm^2 at

wavelength of 1050nm and coil diameter of 30cm. An effective are of ~920μm^2 can be achieved when using 50cm coil diameter. There is no significant variation in mode areas when wavelength is changed within the bandgap (see Fig. 3.3).

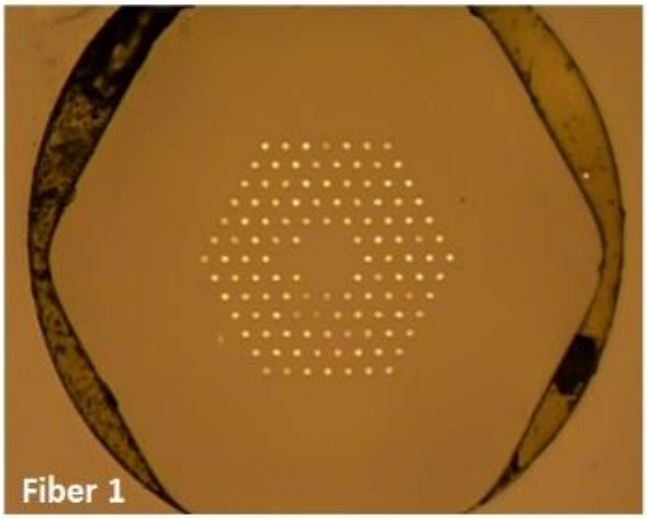

Fig. 3.2 Cross section photos of the two fabricated fibers.

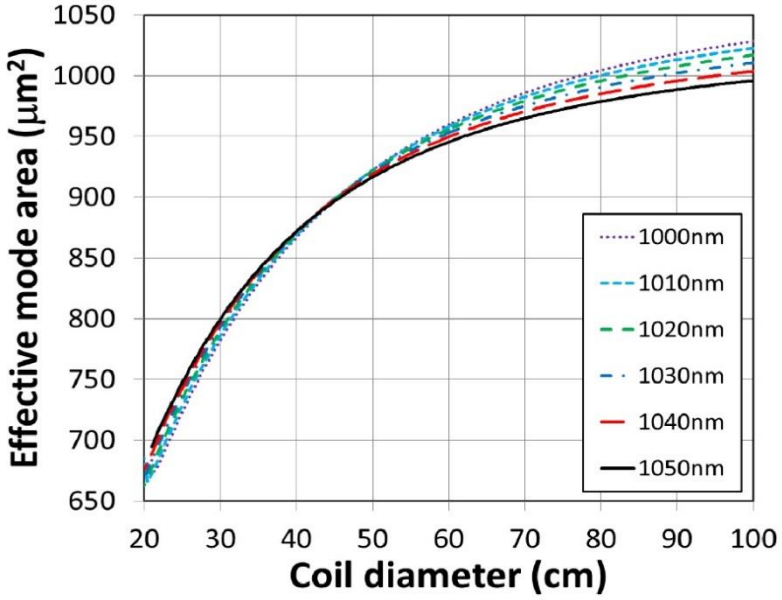

Fig. 3.3 Simulated effective area of Fiber 1 versus coil diameter.

The bend-dependent loss was measured for Fiber 1 by setting the coil diameters to 20cm, 30cm and 35cm and performing cut-back measurements. The result is shown in Fig. 3.4. The target coil diameter is 30cm. At the center of the third bandgap at ~1.05μm, very little bend dependent loss was measured at the target coil diameter. At 20cm, significant bend-induced loss was seen throughout the band. Also shown is the much stronger bend-induced loss in the second bandgap at ~1.55μm. This is expected, due to the shallower band depth for this even bandgap (Fig. 3.1b) [81].

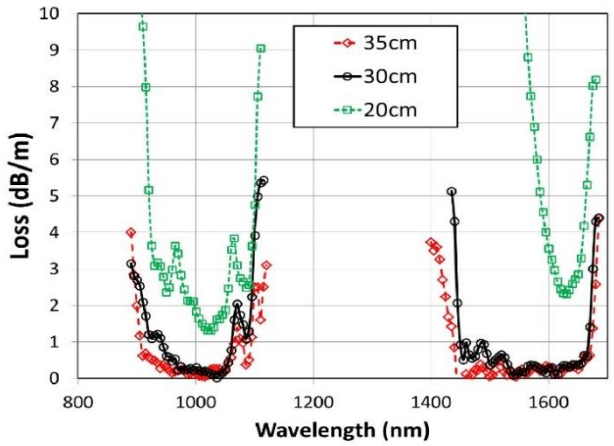

Fig. 3.4 Loss of Fiber 1 at coiling diameters of 20cm, 30cm and 35cm

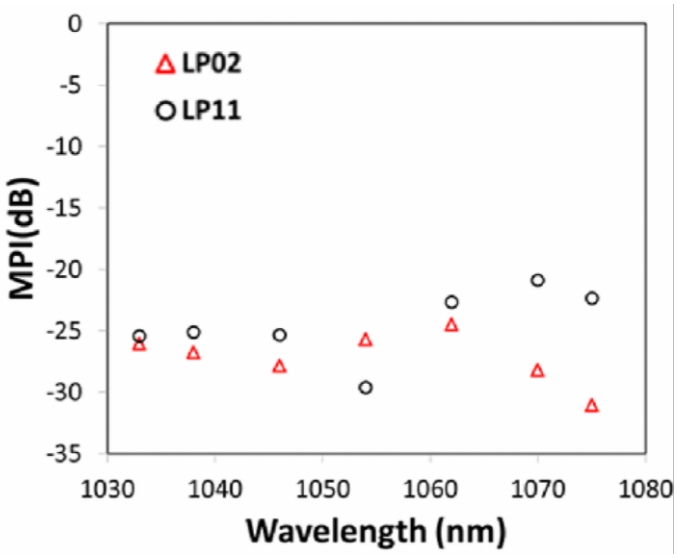

Fig. 3.5 Measured HOM contents in a 5 m fiber coiled at 70 cm diameter using S2 method [7].

The HOM contents are also measured across the bandgap in a 7 m fiber coiled in 70 cm diameter in Fig. 3.5 using a fast S^2 method implemented with a tunable laser and a CCD camera [71]. As it can be seen, the HOM contents are well below 20 dB across the bandgap once the launch is optimized.

3.4 Ytterbium-doped AS-PBF lasers

Two active PBFs with Yb-doped cores were fabricated using the standard stack and draw technique for this work. Both active fibers were drawn from the same preform while the second active PBF (Active2) was ~4% larger than the first active PBF (Active1) in dimensions. This small increment was calculated to allow true single-mode operation at the lasing wavelength. A more detailed explanation will be given in Section 3. For all three fibers, the nodes in the cladding were made of germanium-doped silica with graded index profile which has a peak value of 1.48. Both active PBFs were coated with low refractive index polymer coating, providing a numerical aperture (NA) of 0.46 for the guidance of pump light. The pump absorption of the active PBF was estimated to be ~1dB/m at 976nm. The cross-section of the Active1 PBF and the dimensions of three fibers are shown in Fig. 3.1 and Table. 3.1, respectively.

Table. 3.1 Dimensions of fabricated PBF

PBF	Pitch/Λ (μm)	Node Size/d (μm)	d/Λ	Core size flat to flat (μm)	Core size corner to corner (μm)	OD flat-to-flat (μm)	OD corner-to-corner (μm)
Active1	16.41	6.56	0.4	48.14	56.66	404.52	439.06
Active2	16.96	6.71	0.4	50.07	58.83	417.5	454.3
Passive	16.52	6.37	0.39	49.46	58.08	405.01	440.15

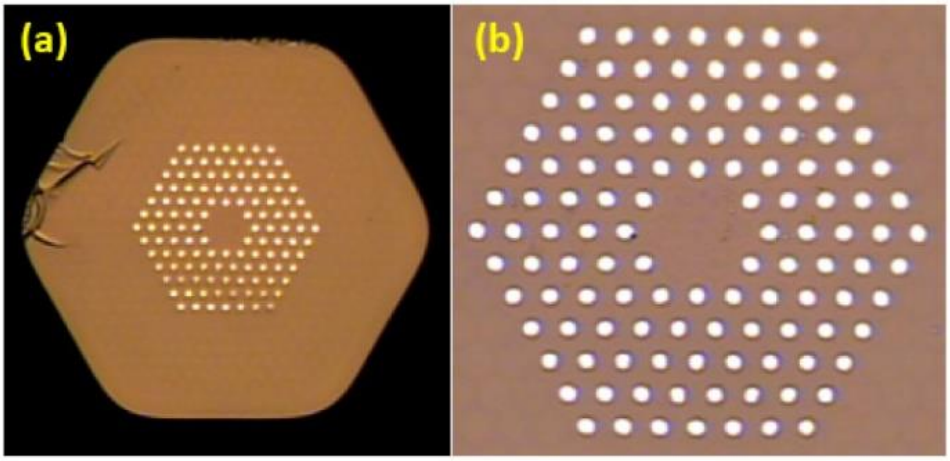

Fig. 3.6 (a) Cross-section of the Active1 PBF; (b) Zoomed-in cross-section of Active1 PBF.

The core of the active PBFs consists of 7 Yb-doped rods in the center. Ideally, the refractive index of the active rods should be matched to that of silica background. However, this is very hard to satisfy and our active rods have a small index depression relative to silica [86]. In order to determine the index depression Δn which is defined as the difference of refractive index between the background glass and the active rods, the fiber was cladding pumped well below the lasing threshold and the mode pattern was measured using amplified spontaneous emission (ASE). This was then compared to the simulation, as done in [58]. The simulation studied mode profiles at different index depression Δn, ranging from 0.5×10^{-4} to 3×10^{-4} with increment of 0.25×10^{-4}. The mode patterns and the intensity distributions across the white axis are presented in Fig. 3.6. A shallow dip at the center of the core was observed during the experiment due to the index depression. The simulation showed this phenomenon clearly. It is estimated that the measurement best matches simulation result when Δn equals 2.25×10^{-4}.

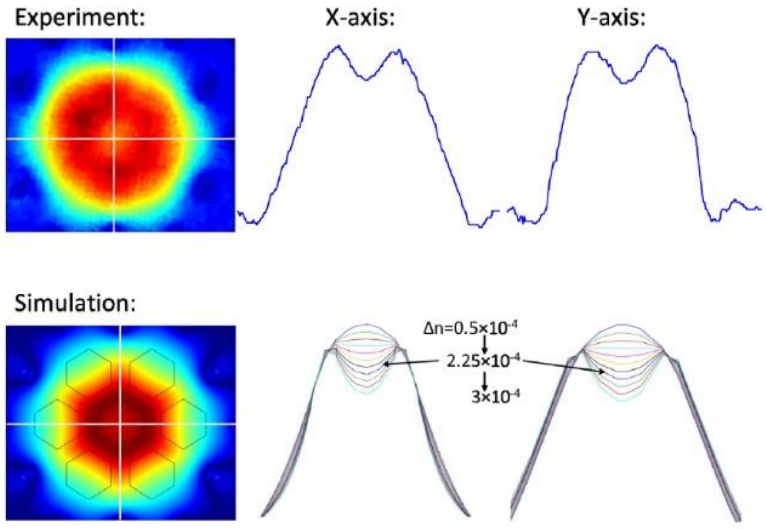

Fig. 3.7 (a) Top: Experimental results of mode profile and intensity distribution using ASE; (b) Below: Simulation of mode profile at Δn = 2.25 × 10−4 and intensity distributions at various Δn with 0.25x10−4 increments.

The depressed refractive index of the Yb-doped rods would directly affect the effective mode area of the non-Gaussian-like mode. Figure 3.3a shows the effective mode area with respect to the index depression in a straight fiber. As the difference in refractive index increases, the FM becomes flatter, resulting in a larger effective mode area. At an index depression of 2.25×10^{-4}, the effective mode area reaches ~1450μm^2. .On the other hand, the effective mode area at various bending radii when Δn is fixed at 2.25×10^{-4} is plotted in Fig. 3.3b. At a bending radius of 0.25m, which is the designed coil configuration, the effective mode area is estimated to be ~1020μm^2.

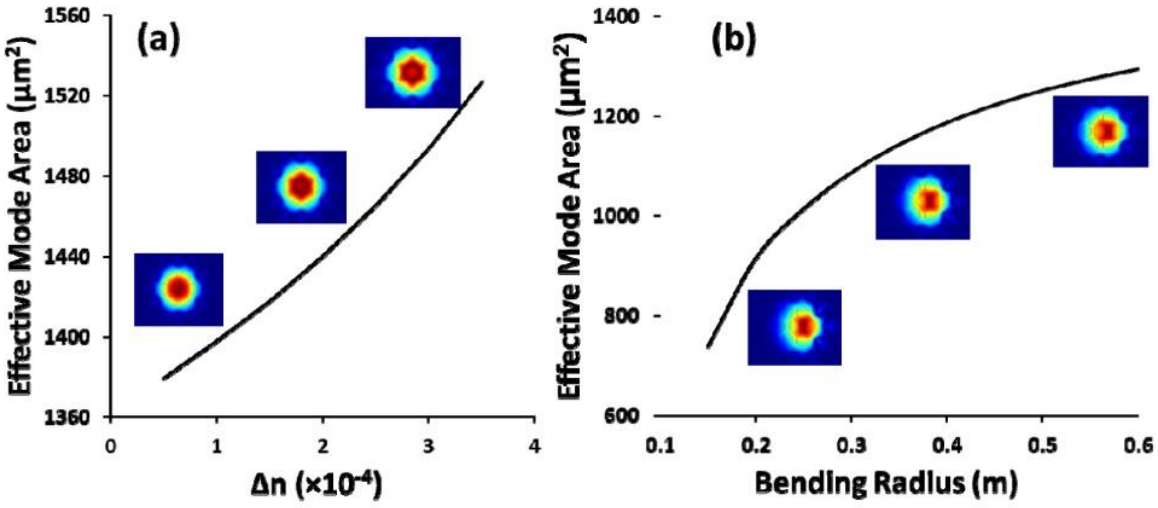

Fig. 3.8 (a) Simulated effective area versus index depression Δn in a straight fiber; (b) Simulated effective area versus bending radius with $\Delta n = 2.25 \times 10^{-4}$.

The two active PBFs were subjected to extensive study to determine the power scalability and robustness of single mode operation. In all the characterizations, the fiber had both ends perpendicularly cleaved to form the cavity and was laid in an aluminum groove with a 50cm diameter coil in accordance to the initial design. The metal plate also served to dissipate heat from outside coating. The fiber was cladding pumped by a commercial laser diode emitting at ~976nm (LIMO200-F200-DL980) through a dichroic mirror. The output power at 1030nm and the residual pump light were measured at the other end. The slope efficiency with respect to the absorbed pump power and lasing threshold as a function of bending diameter using 6m Active1 is shown in Fig. 3.4a. The slope efficiency remained above 80% with the threshold below ~6W when bending diameter was kept at and above 50cm. It can be seen that from a bending diameter of 60cm to 50cm, the slope efficiency only dropped 3%, but the mode quality is expected to benefit from a tighter coil size. The optimal coil size was consequently determined to be ~50cm.

The Active1 was then repeatedly cut back from its original length. The slope efficiencies versus fiber length are shown in Fig. 3.4b. The dashed blue line indicates the slope efficiency with respect to the launched pump power while the solid red line indicates the slope efficiency with respect to the absorbed pump power. Both efficiencies increased as the fiber length was shortened until they reached maximal values of 72% and 83% at the optimal fiber length of 5.2m.

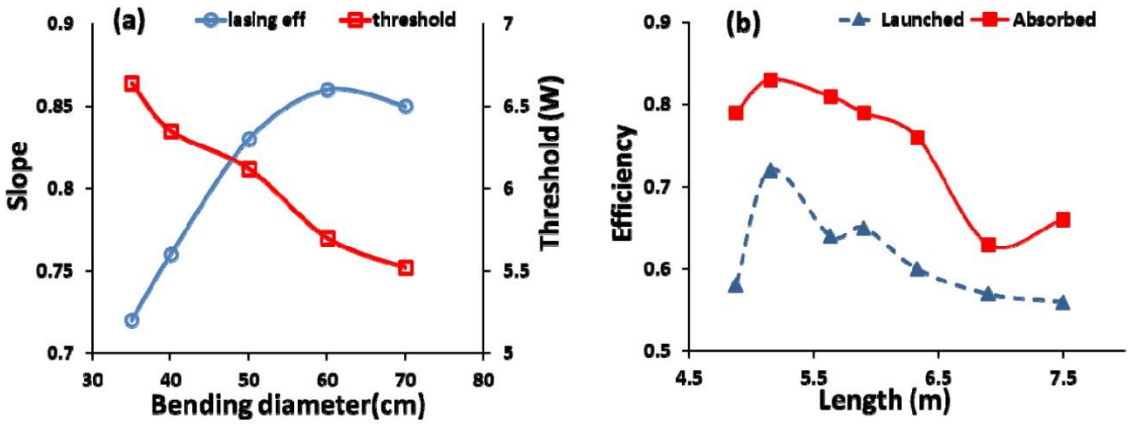

Fig. 3.9 (a) Efficiency relative to the absorbed pump as a function of bending diameter. (b) Measured optimal fiber length to achieve maximal efficiency.

However, a closer look shows that Active1 did not provide single-mode operation very well at 50cm coil diameter. This was attributed to the lasing wavelength being too close to the low frequency edge of the bandgap, where the fiber is multimode [23]. The Active2 PBF with 4% increase in dimension was drawn to aim at moving the lasing wavelength of ~1030nm closer to the high frequency edge of the bandgap, where robust single-mode operation is expected (see Fig. 3.6). Laser output from a section of 6m Active2 coiled at 50cm in diameter was characterized for beam quality. A CCD camera traced the

output beam propagation over 15cm distance. Calculation of the beam size was based on the second-moment method, yielding M^2 = 1.13 and M^2 = 1.16 along the horizontal and vertical direction respectively. The fact that M^2 is larger than 1 is attributed to the non-Gaussian-like beam shape. The promising result shown in Fig. 3.5(a) implies robust single mode operation. The expected rotation of the hexagonal mode shape from near field to far field can be clearly observed. The slope efficiencies of Active2 were measured subsequently. The slope efficiencies relative to the launched and absorbed pump power were measured to be 70% and 84% respectively, which is close to the maximum efficiencies of Active1. The highest output power achieved in this configuration was ~75W, limited by the pump power available.

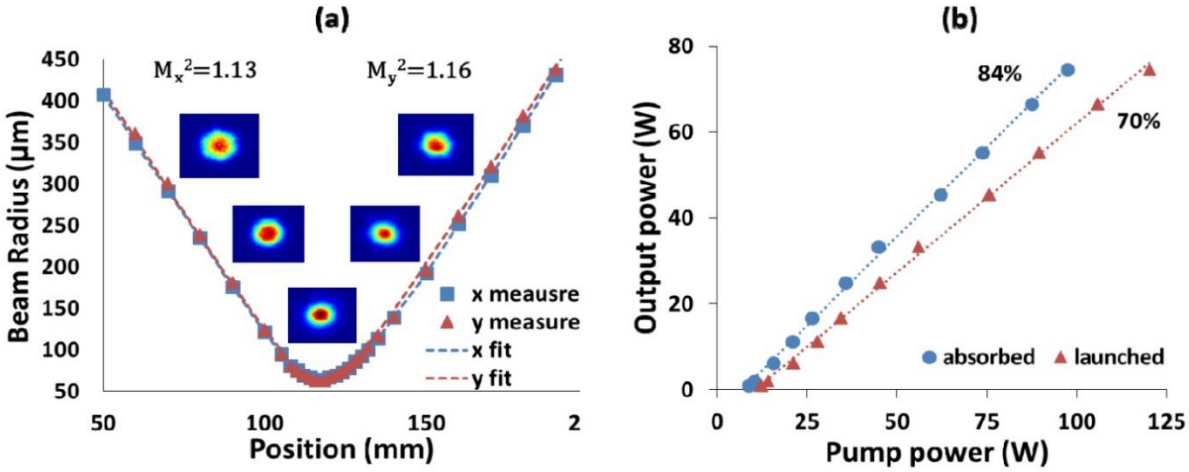

Fig. 3.10 (a) Beam quality measurement of the output signal. Insets along the curve represent mode profiles at near-field, beam waist and other transition phases. (b) Measured slope efficiencies relative to the launched and absorbed pump power. The dotted line represents a linear fit while the solid circles and triangles represent measured values.

As mentioned before, by bringing the high-frequency bandgap edge closer to the laser wavelength, one can expect more robust single-mode operation. This can be

illustrated by the inset in Fig. 3.6, as the frequency increases, the HOMs are cut off gradually at the high-frequency bandgap edge and only FM is supported at the highest frequency [87]. To test the robustness of the single-mode operation, the light from a tunable laser was launched into a section of Active2 with only a single 50cm coil. The launch beam was first carefully aligned then intentionally moved by 6.25μm and 12.5μm in the transverse plane off the optimal launch condition so that HOM may be excited. Fig. 3.6 shows the scaled transmission band obtained from the passive PBF and mode profile captured from Active2 at various wavelengths from 1025nm-1095nm. Since the index depression of the active fiber is very small, we expect its bandwidth to be only slightly narrower than that of the passive fiber while the overall bandgap structure remains the same. Near the short wavelength edge of the bandgap, i.e. at the high frequency edge of the bandgap, the fiber exhibited a clear robust single-mode regime in Active2. HOM was observed at non-optimal launch conditions above 1040nm.

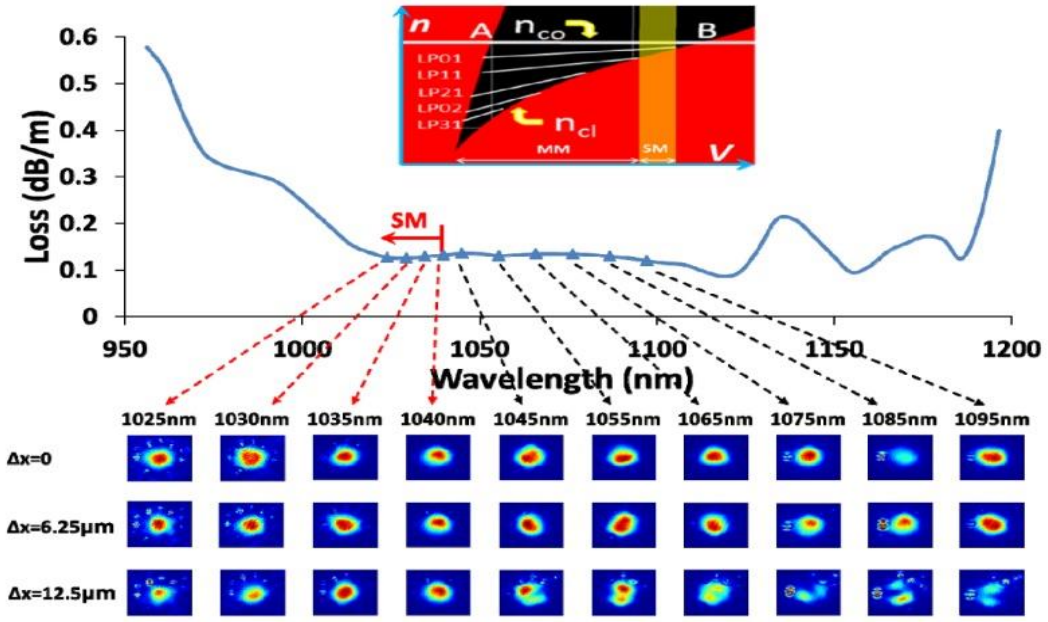

Fig. 3.11 The transmission band measured from the passive PBF and the measured mode profile from Active2 at different wavelengths. Δx is distance of the launch offset. The inset illustrates modes supported within the bandgap of a PBF.

3.5 Conclusion

Fibers with strong higher order mode suppression are critical for further power scaling of single mode fiber lasers to beyond kW levels. In an all-solid photonic bandgap fiber, modes are only guided due to anti-resonance of cladding photonic crystal lattice. This provides strongly mode-dependent guidance, leading to very high differential mode losses. In addition, the all-solid nature of the fiber makes it easily spliced to other fibers. We have studied both theoretically and experimentally the possibility of further mode area scaling using all-solid photonic bandgap fibers. We confirmed that all-solid photonic bandgap fibers have the potential to provide significant higher order mode suppression. For the

passive AS-PBF, we have demonstrated a record effective mode area of ~920μm^2 with higher order mode content below −30dB.

We then have demonstrated an Yb-doped all-solid PBF laser with a core diameter of ~50μm. The effective area is ~1450μm^2 in a straight fiber and ~1020μm^2 when coiled at 50cm diameter. The large effective mode area will help to mitigate nonlinear effects at high powers. Active1, reached 83% and 72% slope efficiencies against the absorbed and launched power respectively. Active2 reached 84% and 70% slope efficiencies with respect to the absorbed and launched power respectively. We have also confirmed robust single-mode operation in Active2 with M^2 less than 1.2 in both horizontal and vertical axes. We have also experimentally confirmed that the single-mode regime exists at shorter wavelengths close to the edge of transmission window and small fiber diameter adjustments can be used to fine tune the robustness of single mode operation, a feature unique to PBF. This work demonstrates that the significant power scalability and excellent beam quality is possible in all-solid PBF lasers.

CHAPTER FOUR

MULIPLE-CLADDING-RESONANCE ALL-SOLID PHOTONIC BANDGAP FIBERS WITH LARGE MODE AREA

4.1 Introduction

In the course of developing high-power fiber lasers, mode area scaling is a key to mitigate nonlinear effects as a result of high optical intensity. In many applications, diffraction-limited beam is highly desired. We now know that mode instability can lead to poor mode quality at higher powers even in fibers with some higher-order-mode suppression. In the recent decade, numerous approaches have been proposed, which led to a significant progress in mode area scaling of optical fibers. One notable area is in photonic crystal fibers (PCF) [34,53,59,88,89]. The short straight PCF rods used in the demonstrations have prevented their use in multi-kilowatts fiber lasers due to limited heat dissipation. The air holes in the cladding have also prevented them from being used in robust monolithic fiber lasers. The lack of strong higher-order-mode suppression has also led to mode instability issues [32,57,86]. To overcome some of the drawbacks, we have studied all-glass and coil-able leakage channel fibers (LCF) [57,68]. In the light of recent works in mode instabilities, much stronger higher-order-mode suppression is necessary to ensure single-mode operation at high powers [33,36].

Recently there have been significant interests in all-solid bandgap fibers (AS-PBF) [62,66,90]. The unique combination of an open cladding and a dispersive anti-resonant cladding which enhances the mode dependence enables some of the strongest

higher-order-mode suppressions. In a recent work, we have demonstrated the existence of a robust single-mode regime near the short-wavelength edge of the bandgap in an ytterbium-doped 50μm-core all-solid photonic bandgap fiber. Our efforts in further mode area scaling of all-solid photonic bandgap fibers using similar designs have failed to find a design with sufficient higher-order-mode suppression for 100μm-core fibers. This led us to look for significant improvement in the designs.

It is well known that additional cores in the cladding which are in resonance for coupling with the higher-order modes in the main core can be used to suppress the higher-order modes in the main core [54,91]. This has even been recently used in hollow-core photonic bandgap fibers for suppressing higher-order modes [92,93]. Recently, it has been suggested that multiple-coupled cores in the cladding can lead to much improved higher-order-mode suppression [94]. The key improvement is the use of multiple coupled small cores in the claddings which both enhances the coupling with higher-order modes in the main core and broadens the coupling resonance. The higher-order-mode in the main core is coupling to multiple coupled cores in the cladding simultaneously in the new design instead of just few isolated cores in the cladding in previous works. Narrow coupling resonance in the previous approaches has always made them somewhat impractical [54,91]. Such multiple coupled cores can be easily incorporated in the existing fabrication process of photonic bandgap fibers. The new proposal is, therefore, significant in providing a far more practical design. Recently, robust single-mode operation with mode field diameter of 44μm in a straight fiber was demonstrated using this approach in an all-solid photonic bandgap fiber [95].

In this chapter, we theoretically and experimentally investigated the multiple-cladding-resonance (MCR) designs in all-solid photonic bandgap fibers for further mode area scaling as well as for coiled operations. Detailed numeric studies have been conducted for multiple cladding designs. Our simulation also indicates well over two orders of magnitude suppression of higher-order modes in coiled operations. We have demonstrated robust single-mode operation with record effective mode area of ~2650μm^2, i.e. a mode field diameter of 58μm, in straight fibers. This represents a significant improvement over previous demonstrations of robust single-mode operation in all-solid photonic bandgap fibers.

4.2 Design theory

Additional smaller cores can be easily created in the cladding of photonic bandgap fibers by missing several nodes. The smaller cores share the same cladding as the main core. If the cladding cores are well isolated, the resonant conditions between the fundamental mode in the cladding cores and various higher-order modes of the main core can be easily calculated. Using step-index fiber analogue, the propagation constant of modes in the main core can be written as:

$$\beta_m^2 = k^2 n_b^2 - \frac{U_m^2}{\rho_m^2} \tag{1}$$

where k is the vacuum wavenumber; n_b is the refractive index of the background glass; ρ_m is the main core radius; and main core parameter U_m is as normally defined for optical fibers [96]. It needs to be noted that the refractive index of all the cores is the same as that

of the background glass n_b in this case. Similarly, the propagation constant of modes in the cladding cores can be written as

$$\beta_c^2 = k^2 n_b^2 - \frac{U_c^2}{\rho_c^2} \tag{2}$$

The cladding core parameter U_c is defined similarly as U_m. The resonant condition for maximum coupling of a mode in the main core and a mode in the cladding core is $\rho_m = \rho_c$. Using the relations obtained thus far in Eq.1 and Eq.2, the resonant condition can be written as:

$$\frac{U_m}{\rho_m} = \frac{U_c}{\rho_c} \tag{3}$$

Since the refractive index of core and cladding are the same for both main and cladding cores. The resonant condition can be rewritten using the normalized frequency, i.e. V value, V_m and V_c for the main and cladding cores respectively.

$$\frac{U_m}{V_m} = \frac{U_c}{V_c} \tag{4}$$

This can be easily calculated for the fundamental mode of the cores in the cladding and various higher-order modes in the main core (see Fig. 4.1).

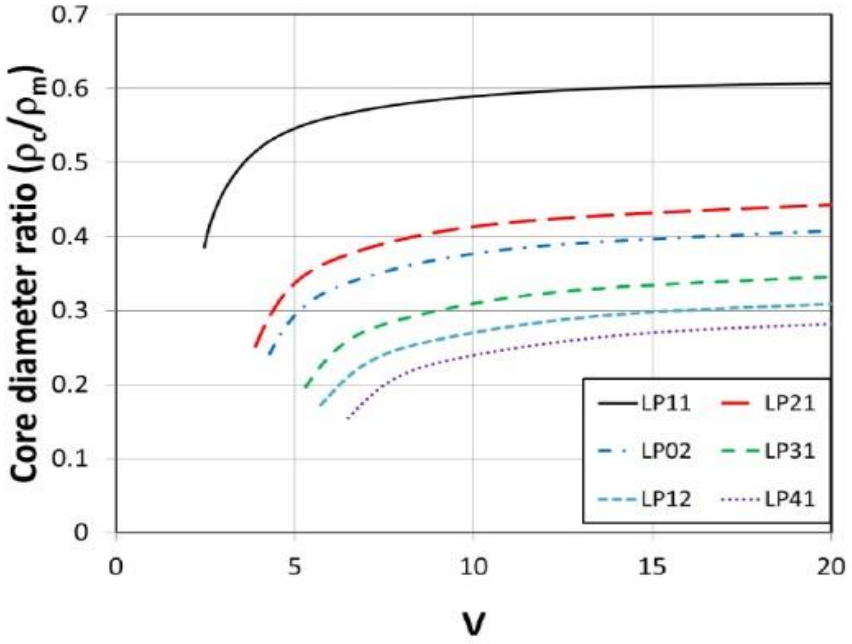

Fig.4.1 Required core diameter ratio (ρ_c/ρ_m) for maximum resonant coupling between the fundamental mode of the cladding core and one of the higher-order modes of the main core versus normalized frequency (V value) of the main core.

The horizontal axis is the V value of the main core. For weakly coupled cladding cores, Fig. 4.1 provides a reasonable approximation for a straight fiber. In the multimode regime with V>10, for coupling with LP_{11} and LP_{21} modes in the main core, $\rho_c/\rho_m \approx 0.6$ and 0.44 respectively. As it turned out, this approximation works reasonably well for cladding cores of a photonic bandgap fibers.

4.3 Numeric simulations and results

Based on the approximation in Fig. 4.1 as guidance, three cladding designs were numerically studied using a FEM mode solver. The cross-sections of all designs are shown in Fig. 4.2. For all the designs, a 7-cell core is adopted. Instead of the periodically arranged high-index inclusions surrounding the core, several cladding structures are used to form

the cladding. The smaller cores in the cladding are formed by purposefully taking out a certain number of nodes such that a cladding defect core is created. The first design shown in the left side of Fig. 4.1 is referred to the "mixed-cell" since it has two and three nodes removed to create the cladding cores. The second and third design shown in the middle and right side of the Fig. 4.2 are accordingly referred to "three-cell" and "two-cell" respectively. The core diameter ratio $\rho_c/\rho_m \approx 0.65$ and 0.53 for the 3- and 2-cell cores respectively, close to the 0.6 required in Fig. 4.1 for coupling with LP_{11} mode in the main core. It is worth noting that the effective mode index of the cladding core will increase or decrease in a coiled fiber depending on its relative location to the center of the coil. The condition required in Eq. 4 is, therefore, only an approximation in this case.

The nodes in the cladding were made of germanium-doped silica with a graded index profile similar to the one used in our previous Yb-doped PBF. The pitch, that is the distance between two adjacent cladding nodes, is 25μm, which yields a 100μm core diameter. The ratio between the diameter of the cladding nodes and pitch is fixed, at 0.24.

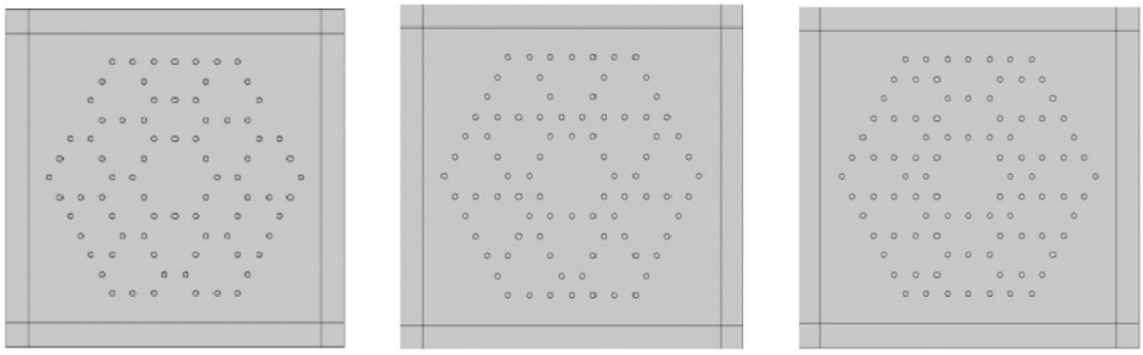

Fig. 4.5 Cross-section of PBFs studied. From left to right are: mixed-cell, three-cell and two-cell AS-PBF.

A commercially available COMSOL Finite Element Method (FEM) mode solver is used for the simulation. A perfectly matched layer is implemented to obtain the mode loss. The fiber is simulated under 50cm bending radius. This provides a coil diameter which is acceptable for multi-kw high-power fiber lasers and minimizes mode compression due to coiling. The wavelength is scanned from 900nm to 1100nm. Given the symmetry of the cladding arrangement, propagation loss under different bending orientations has been studied. The arrow in the inset of Fig. 4.3 indicates the direction where the center of the coil is. The loss curves with respect to the wavelength are plotted in Fig. 4.3.

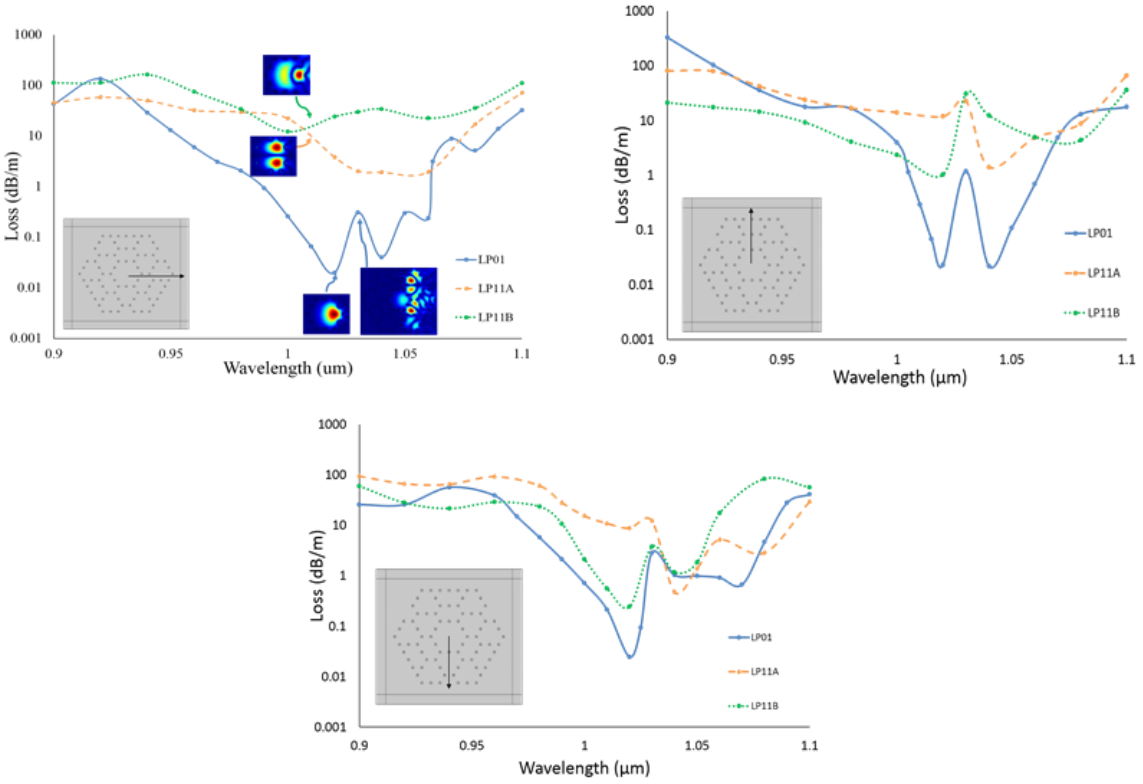

(a)

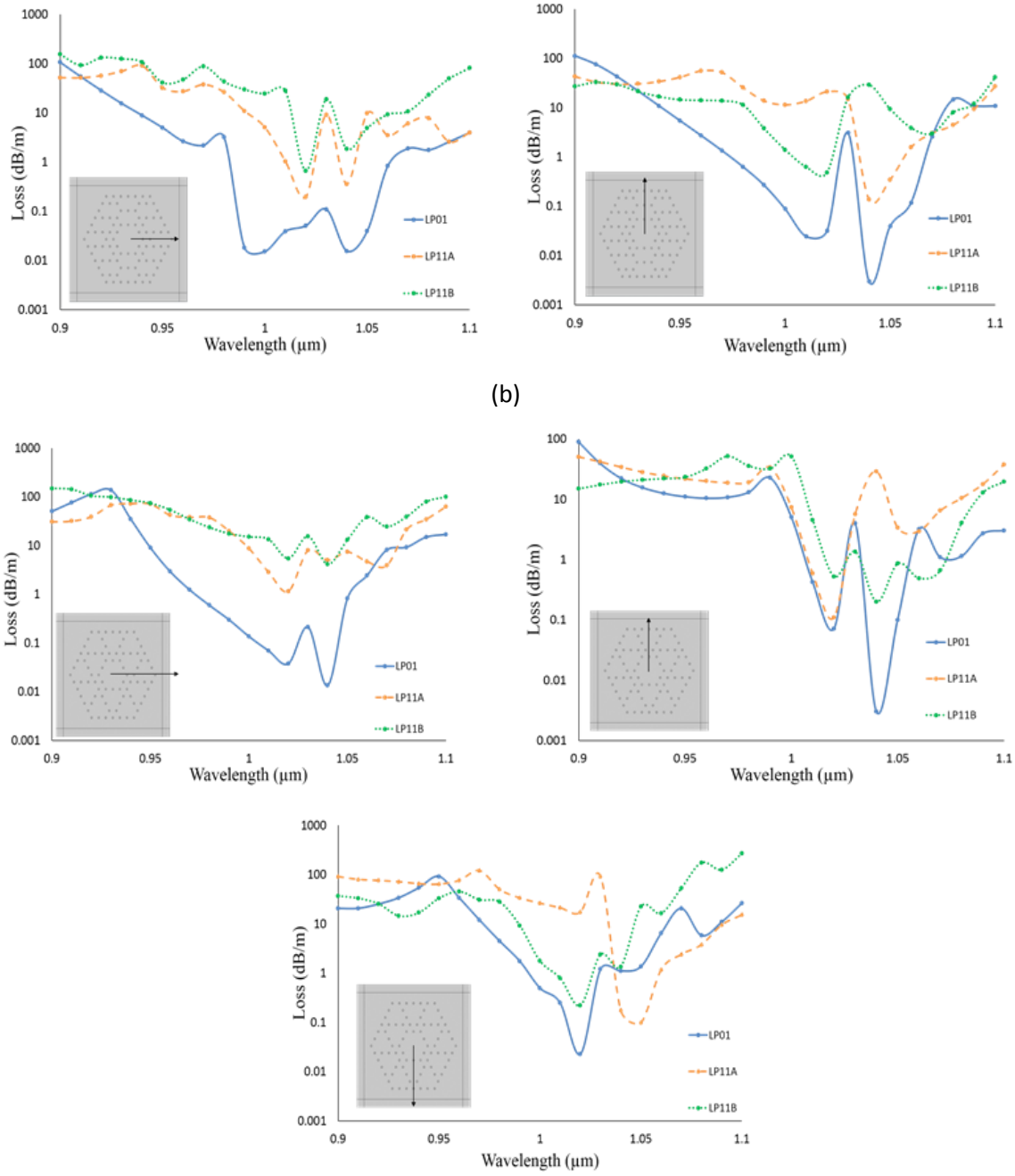

Fig. 4.3 Simulated loss of LP01 (blue) and LP11 modes (Orange and Green) in (a) mixed-cell design, (b) two-cell design and (c) three-cell design. The insets show the layout of different cladding arrangement. The arrow in the inset indicates the coil center. Insets also show the mode patterns of LP_{01} and LP_{11}.

For the mixed-cell PBF (Fig. 4.3a) and three-cell PBF (Fig. 4.3c), each has three possible different bending orientations: one horizontal and two vertical. Meanwhile two-cell PBF only has two fundamentally different ways to coil. The first three dominant modes, namely LP_{01} and LP_{11} ($LP_{11}A$ and $LP_{11}B$) with two orthogonal orientations are presented. The inset in Fig. 4.3a shows the generic mode pattern for LP_{01}, $LP_{11}A$ and $LP_{11}B$. It can be clearly seen that when fiber is bent horizontally, all three designs demonstrate significant differential mode loss within the third bandgap at wavelength ranging from 1000nm to 1030nm, which indicates a possible window for single-mode operation. The lowest fundamental mode loss can be as low as ~0.01dB/m.

One should note that at 1030nm the FM tends to have a small loss peak, which can be attributed to the resonance effect with the cladding, as it can be clearly seen in the inset of Fig. 4.3a. The differential loss is much worse when bending vertically. For example, for the three cell PBF shown in the Fig. 4.3c, the $LP_{11}A$ mode has almost the same loss as LP_{01} mode does. At longer wavelengths, it can even have less loss than LP_{01} mode. The loss of all LP modes tend to increase significantly outside the bandgap when the wavelength is below 1000nm or beyond 1050nm. The mode can be severely distorted in the high loss regime.

Table. 4.1 Summary of loss ratio for three types of fiber design

Fiber Type	Wavelength (nm)	Minimum FM loss (dB/m)	Corresponding HOM loss (dB/m)	Loss ratio
Mixed-cell	1020	0.02	3.83	192
Three-cell	1040	0.01	4.13	413
Two-cell	1000	0.02	5.03	252

Table. 4.1 summarized the FM loss, minimum HOM loss and loss ratios at the wavelength that has the minimum FM loss for the horizontally coiled fibers. Note that the corresponding HOM loss is picked between LP11A and LP11B, whichever has the lower loss. From the table, it can be seen that the three-cell PBF has the highest loss ratio at 1040nm but the bandwidth for low FM loss is rather narrow in this case. The two-cell PBF has the second highest loss ratio, yet the LP11 mode loss drops down dramatically once the wavelength is longer than 1000nm. It is worth noting that, as for the mixed-cell fiber design under horizontal bending, both LP11A and LP11B mode loss are above 10dB/m while the fundamental mode loss is kept at or below 0.2dB/m around 1000nm. In addition, the bandwidth for such high differential loss is broader compared to the three-cell and two-cell designs. As the wavelength move toward 1020nm, the LP01 continues to drop below 0.1dB/m, even though the LP11A mode loss simultaneously decreases, the loss ratio between the LP11 to LP01 still reaches as high as 192 (see Table. 4.1).

Ideally, the bending orientation should be controlled to be horizontal for best HOM suppression. However, in practical cases, the bending direction may be arbitrary, meaning a fiber can have a combination of all the possible bending orientations throughout its length. In this case, total HOM loss will be an average loss of all the orientations. Since FM loss remains largely independent of the orientations, it is still sufficient to realize single transverse-mode operation over a few meters of fiber although with a lesser HOM suppression.

4.4 Experimental characterization of MCR PBF

To validate the simulation, the mixed-cell design was fabricated through standard stack-and-draw process. The dimension of the fiber is illustrated in Table. 4.2 and the cross-section of the actual fiber is shown in Fig. 4.4. One can notice that there is a slight difference between actual dimension and numeric simulation, which can be attributed to parameter control during the fabrication. The germanium nodes in the cladding have the same refractive index profile as the one used in the simulation. The center core is made of silica. The outer shape of the fiber is rounded hexagon, which also helps increase the differential mode loss.

Table. 4.2 Dimensions of fabricated hetero-structured PBF

Pitch/Λ (μm)	Node Size/d (μm)	d/Λ	Core size flat to flat (μm)	Core size corner to corner (μm)	OD flat-to-flat (μm)	OD corner-to-corner (μm)
24.8	6.6	0.27	82.3	91.7	411.1	421.3

Transmission, mode pattern and beam quality of the mixed-cell PBF have been fully characterized. In all measurements, the fiber is bent at diameter of 1m, conforming to the bending radius set in the numeric simulation. It is also worth mentioning that the bending direction was not controlled during the measurement. The transmission of a 4m PBF is shown in Fig. 4.5 in a linear scale. The scanning wavelength ranges from 998nm to 1041nm. The highest transmission peak is observed at the vicinity of 1015nm. Knowing the dimension difference, this is well correspondent to the computational results, which has low attenuation around 1020nm under all three bending configurations.

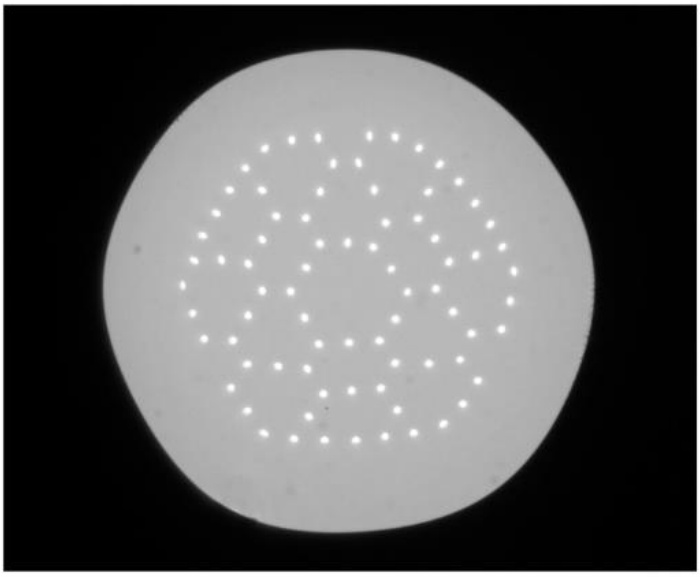

Fig. 4.4 Cross-section of the fabricated mixed-cell PBF.

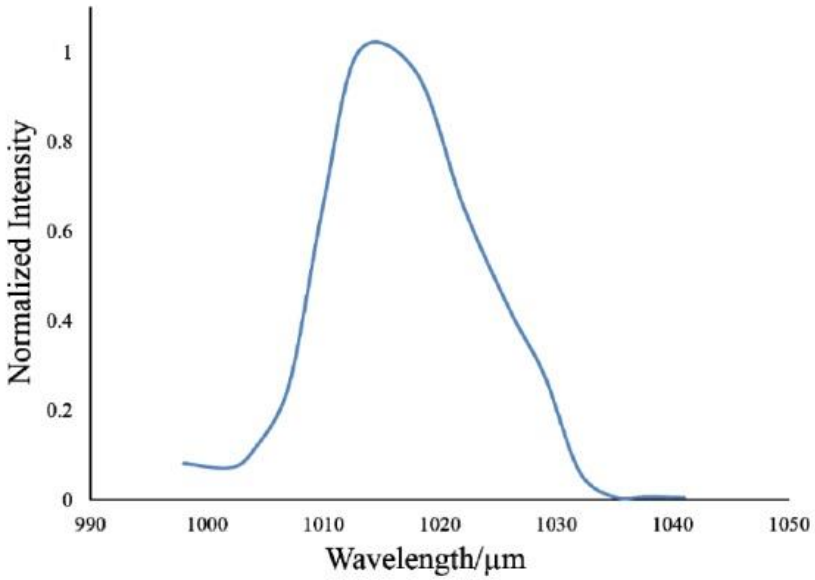

Fig. 4.5 Normalized Transmission of 4m of the fabricated PBF.

The simulated effective mode area (EMA) of the fiber versus bending diameter is shown in Fig. 4.6. At bending diameter of 1m, the EMA is ~1842μm2, marked by the orange diamond in Fig. 4.6.

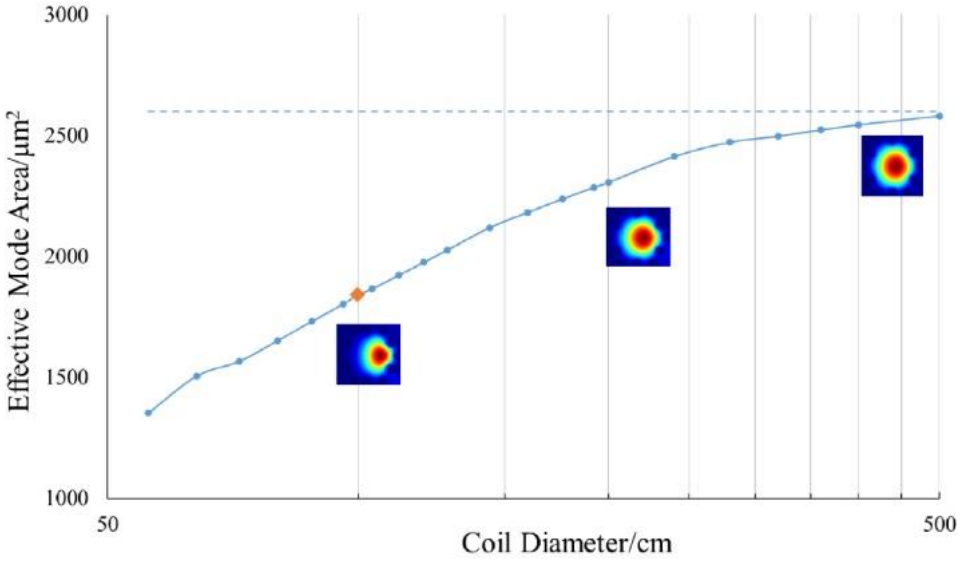

Fig. 4.6 Estimated effective mode area (EMA) of the fabricate PBF. The coil diameter is in log scale. The insets are mode patterns under different coil diameters. At 1m bending diameter, the EMA is estimated to be ~1842μm2, shown as the orange diamond in the chart. The dash line indicates the EMA of a straight fiber.

At large core diameters as in the fabricated fibers in this work, the effective mode indexes of the fundamental and higher-order modes are very close, leading to small intermodal delays. This causes significant difficulty in using the well-known quantitative mode characterization techniques such as S^2 and C^2 techniques [97,98]. Much wide wavelength scan range is required for the S^2 method. In case of the C^2 method, broadband source with coherent length less than few tens of femtosecond is required, in addition to the necessary dispersion compensation. Recently we have demonstrated the first quantitative mode characterization in a 100μm-core fiber using a matched white-light

interferometry where dispersion is completely compensated. The fabricated fiber in this work, however, has very narrow transmission band, which makes any quantitative mode characterization impossible [99].

To verify the robustness of single-mode operation, a tunable laser light was launched into a 4m PBF bending at 1m diameter. The fiber was initially aligned such that light could be directly launched into the center core while the tunable laser scanned the wavelength from 1010nm to 1030nm at the increment of 5nm. The near field mode pattern was captured using a CCD camera at the other end of the PBF. Then the fiber was moved off the optimal launching condition by 12μm, 24μm and 36μm sequentially in attempt to excite HOM. After each offset, the tunable laser would repeat the same wavelength scan.

Fig. 4.7 shows the near field mode image under different launching conditions at various wavelengths. At the optimal launching condition, the fundamental mode was well guided from 1010nm to 1015nm and start to degrade slightly at 1030nm. The HOM was constantly absent across the wavelength spectrum as the launching condition was gradually deteriorated from the optimal launching position. This measurement effectively demonstrated the single-mode operation for this PBF.

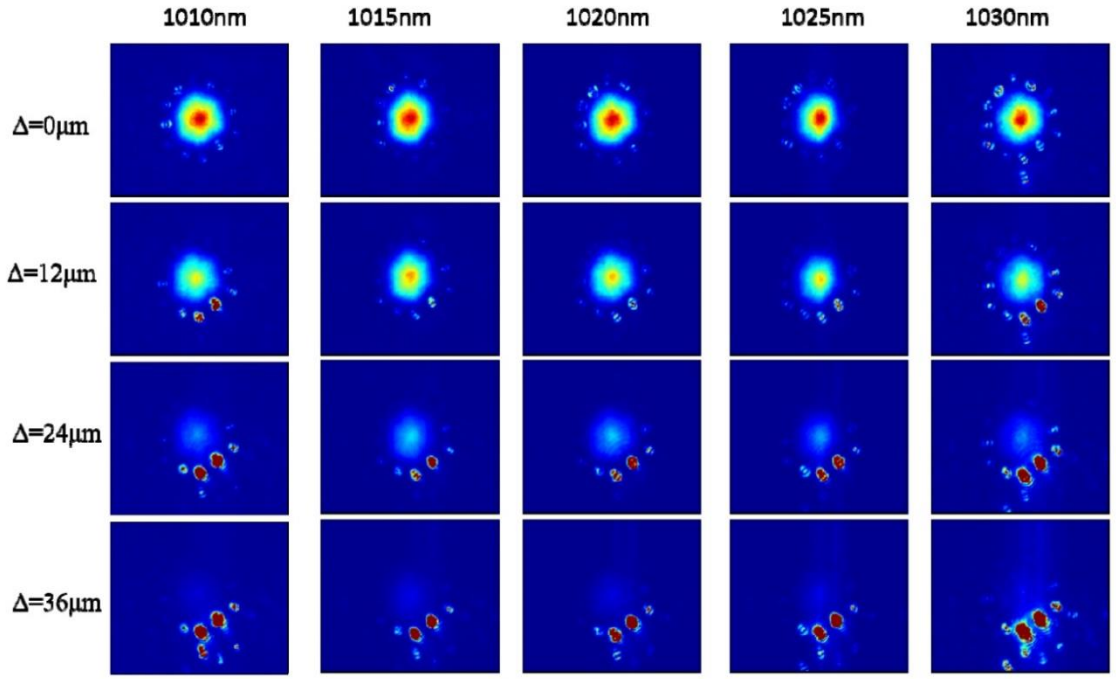

Fig. 4.7 Near filed mode pattern of the mixed-cell PBF at various wavelengths. Δ is the distance of the launch offset.

The beam quality was further verified by employing M^2 technique. Three wavelengths from the tunable laser, namely 1013nm, 1018nm and 1024nm were selected for this measurement. The fiber length and coil diameter are the same as the ones in the tests mentioned above. A CCD camera is deployed to trace the propagation of the output beam. The results are shown in Fig. 4.8. It can be seen that for all the three wavelengths, the measured M^2 values along the horizontal and vertical direction are equal or less than 1.08. The beam profiles captured also indicate a good single-mode operation. This further confirms that robust single-mode operation is supported in the large core while HOM is highly suppressed by the outer cladding defects due to coupling.

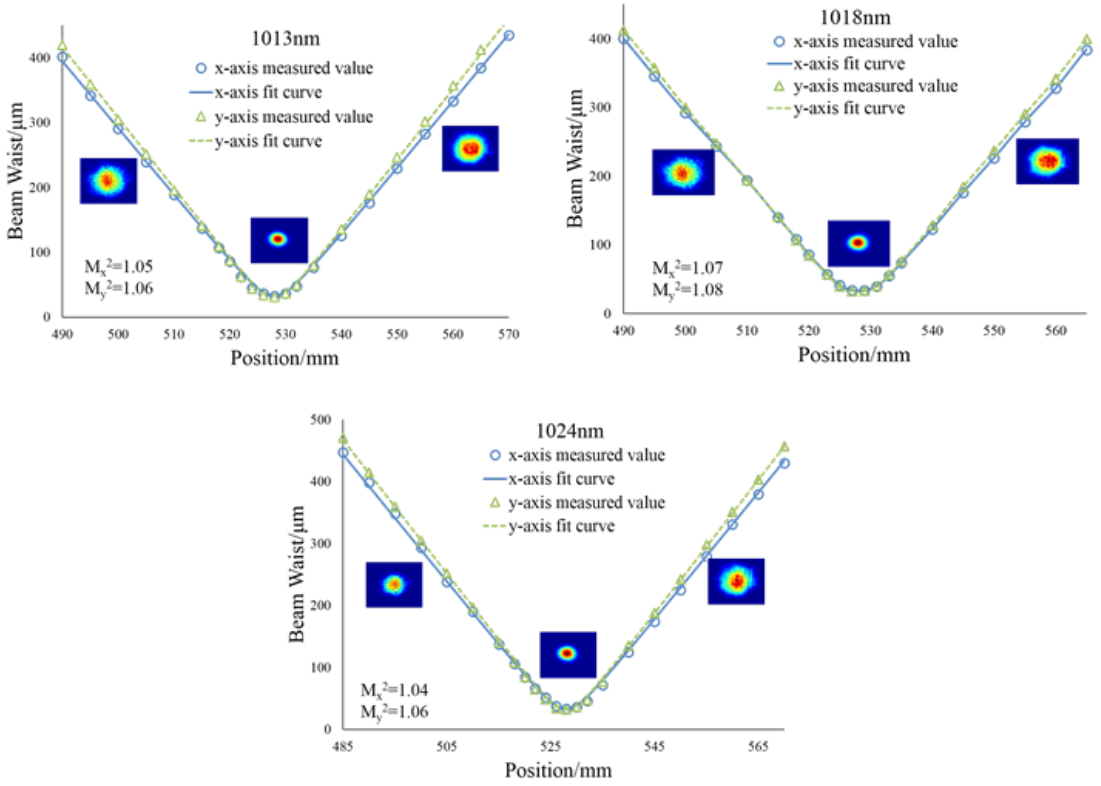

Fig. 4.8 Beam quality measurement at wavelength of 1013nm, 1018nm and 1024nm. Both x-axis (blue) and y-axis (green) were measured with selected mode profiles along the curve.

4.5 Conclusion

In summary, we have demonstrated robust single-mode operation in a MCR-PBF with a record mode area of ~2650μm^2. Three types cladding layouts have been theoretically studied. Comparing among different bending orientations, horizontal bending performs much better in terms of differential mode loss than that vertical bending does. With controlled bending configuration, a very high loss ratio between LP_{11} and LP_{01} can be realized. Mixed-cell design was fabricated and demonstrated to be robustly single-mode at coil diameter of 1m. The M^2 was measured to be less than 1.08 across the bandgap. This

work further pushes mode area scaling limit in single-mode all-solid photonic bandgap fibers. The MCR mechanism can be potentially adopted to realize rare-earth doped single-mode fiber lasers with 100μm core diameter.

CHAPTER FIVE

LOW QUANTUM DEFECT YTTERBIUM-DOPED PHOSPHOSILICATE FIBER LASERS

5.1 Introduction

Many advantages of ytterbium-doped fiber lasers such as excellent efficiency, low quantum defect, and readily available high-power pumps have made them an ideal choice for high-power fiber lasers and amplifiers [100,101]. In the previous chapters, power scaling of ytterbium-doped fiber lasers has been extensively studied. Large mode area fibers, such as photonic crystal fiber (PCF), photonic bandgap fiber (PBF), and leakage channel fiber (LCF), have been developed for mitigating nonlinear effects in the course of power scaling.

To date, most high-power ytterbium-doped fiber lasers operate at 1030nm-1200nm. However, many applications such as spectroscopy and laser cooling require shorter operating wavelengths in order to be frequency doubled or quadrupled to the desired wavelengths [102]. Most importantly, multimode high-power fiber lasers operating below 1020nm can be used in a tandem pumping scheme as pumps to reduce quantum defect heating and provide high pump brightness in ytterbium-doped fiber lasers operating at ~10kW. In this high-power regime, single-mode operation becomes much more challenging due to mode instability driven by quantum defect heating [33,34,36]. Thermal management also becomes much more challenging due to the much higher heat load. Multimode 1018nm fiber lasers are key components in the tandem pumping scheme to

provide high brightness pumps and much lower quantum defects in IPG 10kW fiber lasers [13].

However, it is difficult to realize stable and efficient 1000-1018nm ytterbium-doped fiber lasers in conventional ytterbium-doped aluminosilicate host as it requires a large population inversion to reach gain threshold. Stable operation can only be realized by shortening the fiber, which leads to poor pump absorption. One additional challenge is parasitic lasing at the ASE peak of ~1030nm. This can be mitigated by using a fiber Bragg grating to some extent. The relative gain of 1030nm can be calculated using the simple model proposed by Nilsson et al, which is dependent on the pump absorption and clad/core area ratio [103]. The first key factor for high efficiency for a given launched pump power is low inversion required for reaching the lasing threshold. A second key factor is a small cladding-to-core ratio. This effectively lowers signal intensity in a relatively larger core if the cladding is kept the same, allowing a lower pump intensity to maintain a given inversion. Addressing these two factors effectively can further minimize pump power exiting the fiber.

For tandem pumping, high efficiency is clearly critical due to the very high power involved at multiple kW levels. If high efficiency is not critical, ytterbium-doped fiber lasers can be operated from 976nm-1120nm as demonstrated by Royon *et al* [100]. Recently, a number of high-power 1018nm ytterbium-doped fiber lasers have been demonstrated. A 85W ytterbium-doped 1018nm fiber laser with 15μm core and 130μm cladding was reported in [104]. The highest reported power is 309W at 1018nm with an efficiency against the launched pump power of 71% using a double-clad fiber with a 30μm core diameter and 250μm cladding diameter [105].

Phosphosilicate host is known for reaching gain threshold at lower inversion than that required for conventional aluminosilicate host for lasing wavelengths below 1020nm due to its high emission cross section at shorter wavelength [106]. Using an ytterbium-doped phosphosilicate leakage channel fiber with ~50μm core diameter and ~420μm cladding diameter, we have achieved 70% slope efficiency with respect to the launched pump power at 1018nm. The efficiency is similar to what is reported previously for ytterbium-doped fiber laser operating at 1018nm [104,105].

The cladding diameter of ~420μm in our demonstration is, however, much larger than the 250μm and 130μm reported respectively in [104,105]. The much smaller cladding diameters in [104,105] were critical for the much higher pump brightness required to achieve the reported 71% slope efficiency. The much larger cladding diameter in our work demonstrates that much lower pump brightness is required in our fiber. Tandem pumping is only required currently for 10kW single-mode fiber lasers to lower the quantum defect of the output amplifier. The 1018nm fiber laser pumps need to have high enough power to be useful for this application. Currently commercially available pump power in 200μm-core 0.22NA fiber is 500W, while it is 6kW (Laserline) for 400μm-core 0.22NA fiber. This work therefor provides the technical basis for >3kW 1018nm fiber lasers, which will be a key for scaling single-mode fiber lasers to beyond 10kW.

In this chapter, a number of ytterbium-doped fiber lasers operating between 1008nm and 1020nm were constructed, optimized and carefully characterized in order to understand the limit of laser efficiency. For comparison, free-running fiber lasers at 1030nm were also constructed. The performance of the free-running fiber lasers was

carefully characterized for various ytterbium-doped fiber lengths. This study allows us to gain significant insights to what are limiting the laser efficiency.

5.2 Experimental Setup

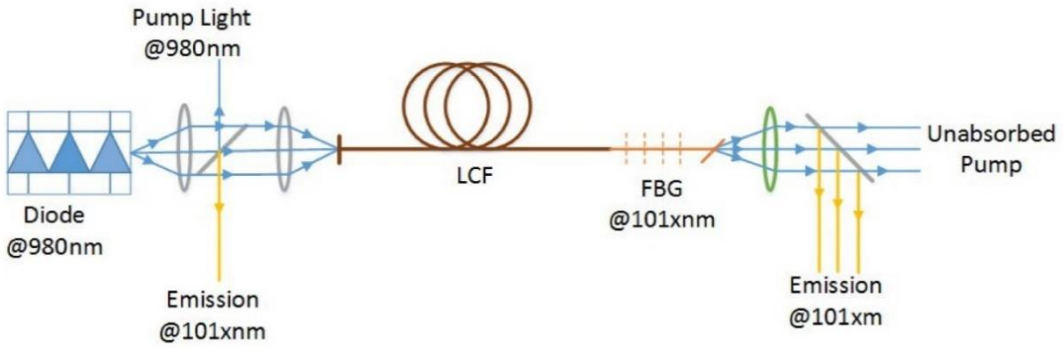

Fig. 5.1 Schematic Experimental Setup.

The configuration of the fiber laser system shown in the Fig. 5.1 consists of a section of Yb-doped phosphosilicate LCF and a FBG with high reflectivity. The Yb-doped LCF used in this system has been previously reported in [58]. The fiber core is 52μm at its smallest dimension (flat-to-flat) and 60μm at its largest dimension (corner-to-corner). The doped area is 30μm in diameter and is made of a highly uniform Yb-doped phosphosilicate glass with an index very slightly below that of silica glass by $2 \times 10{-}4$. The two-layers of features in the cladding are made from fluorine-doped silica glass with a refractive index of 0.0155 below that of silica. The cladding diameter is ~420μm and is coated with a low-index polymer coating (n = 1.375) to guide the pump light with a NA of 0.46. Pump absorption at 975 nm was measured to be 1.05 dB/m. The output mode profile is flat-top instead of Gaussian due to the slight refractive index depression in the core. This

provides an effective mode area of ~1900μm^2 at 1050nm. For high efficiency, it is critical to minimize the intra-cavity splice loss. The photosensitive fiber for the fiber Bragg gratings was specially made at Clemson and has a similar core/cladding dimension of 50μm/400μm as the LCF to minimize splicing loss. A series of FBGs with different reflecting wavelengths were written using an interferometer and a frequency-quadrupled YAG laser in our laboratory at Clemson. It is worth mentioning that the fabrication process is kept constant to ensure the reflectivity for various wavelengths is similar. Due to the inherent nature of the multimode photosensitive fiber, one cannot accurately obtain the reflectivity of the FBG. Fig. 5.2 shows the relative transmission spectrum of a 1018nm FBG. Nearly 20dB of relative transmission loss is achieved at peak of the reflectivity. This measurement is strongly dependent on the excitation of modes in this multimode fiber. It indicates >99% reflectivity for a subset of modes. One end of the FBG is angle cleaved to suppress the ASE while the other end is spliced to the Yb-doped LCF. The Yb-doped LCF is coiled at diameter of 80cm and pumped by 976nm laser diode. Emitted laser lights are recorded at both ends of the fiber.

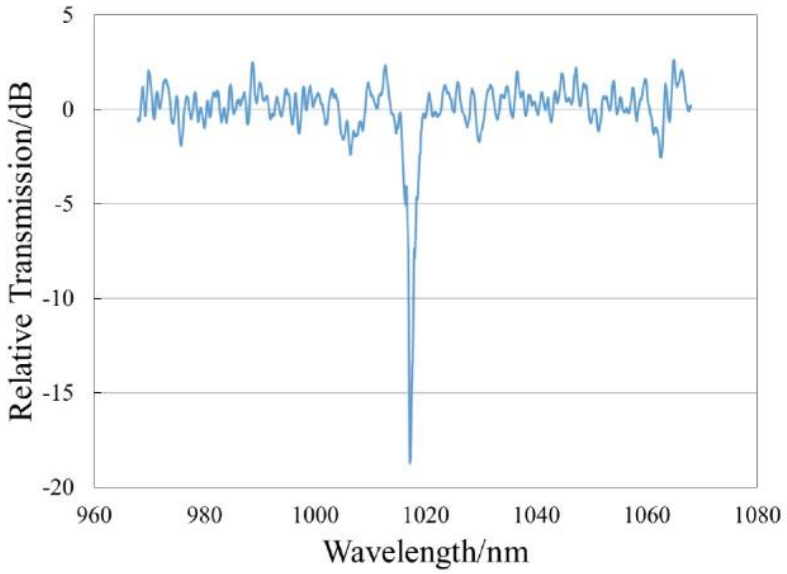

Fig. 5.2 Transmission spectrum of a 1018nm FBG.

To begin with, a 8m Yb-doped LCF and 1018nm FBG is used. However, the ASE is very strong and ultimately lead to spurious oscillation at 1030nm when the pump power exceeds the threshold even though the FBG was angle cleaved. This is because the signal gain at 1018nm was much lower than that at 1030nm at the threshold in the long fiber length used. The fiber was then gradually cut back by 30-40cm each time so that the net gain at 1018nm can ultimately exceed the net gain near 1030nm. Once the fiber laser is operating stably at the desired wavelength and the efficiency is recorded. The FBG is then replaced with a slightly shorter wavelength FBG and the cut-back process was repeated. Fig. 5.3a shows the spectra of the output of all the fiber lasers tested. The laser wavelength ranges from 1008nm to 1020nm. All the spectra are captured at the highest pump power. Over 50dB of difference between signal peak and ASE peak has been achieved for all the wavelengths tested. In particular, as for the 1018nm fiber laser, the laser peak is over 60dB

higher than the ASE peak. By integrating the spectrum, the ASE suppression of 1018nm fiber lasers is calculated to be 41dB. Fig. 5.3b shows the output power of the corresponding fiber lasers versus the launched pump power. The highest output power achieved is 52W at 1020nm when the pump power launched into the fiber reached 82W. The output power is limited by the available pump power. The efficiency is then calculated as 73% with respect to the launched power in this case. The slope efficiency then starts to decrease as lasing wavelength becomes shorter.

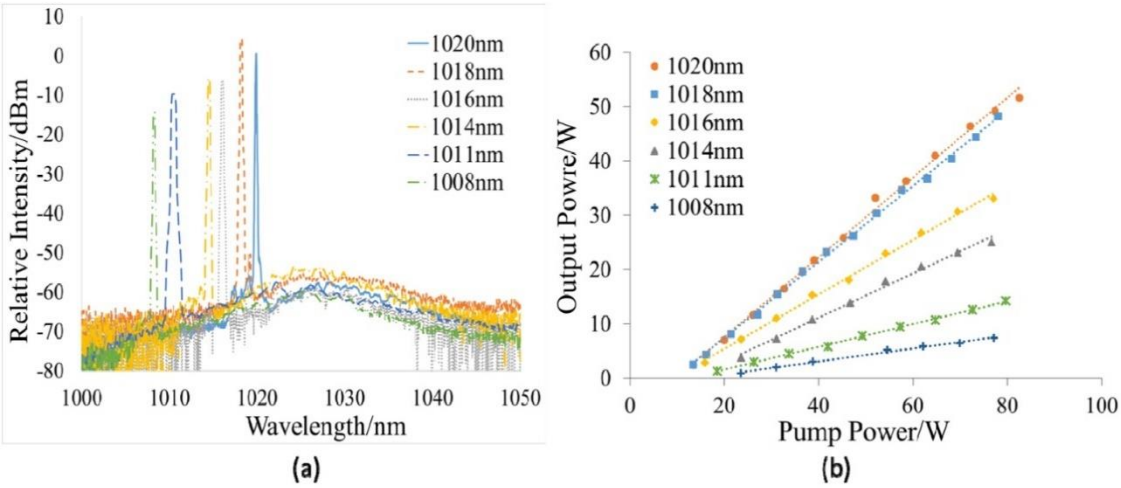

Fig. 5.6 (a) Optical spectra at the laser output, wavelengths ranges from 1008nm to 1020nm. (b) Output powers versus the launched pump powers at various lasing wavelengths.

5.3 Discussions

In this experiment, the fiber length is cut back a small section of length at a time to suppress the ASE until the optimum fiber length is reached for the stable laser operation at the expenses of inadequate pump absorption. As the length of the fiber gets shorter, in order to achieve the same total gain (in our case, round-trip loss is more or less fixed), a higher

average inversion over the fiber length is required to reach the gain threshold. At higher inversions, the ratio of gain at the shorter lasing wavelength over the ASE peak increases. With the help of FBG, the threshold eventually reaches first at the shorter lasing wavelength and the fiber laser will then operate stably. We have conducted this cut-back procedure for several lasing wavelengths between 1008nm and 1020nm. The efficiency of the fiber lasers with respect to the launched pump power and the ytterbium-doped fiber lengths used are shown in Fig. 5.4. It can be seen clearly that the slope efficiency decreases sharply when the operating wavelength is below 1018nm. The decrease of the slope efficiency at shorter lasing wavelengths correlates well with the shorter fiber lengths used at various wavelength. Based on the results in Fig. 5.4 alone, we cannot be sure if the poorer efficiency at the shorter lasing wavelength is due to inadequate pump absorption as a result of the shorter fiber length used or some up-conversion processes at higher inversions or a combination of both.

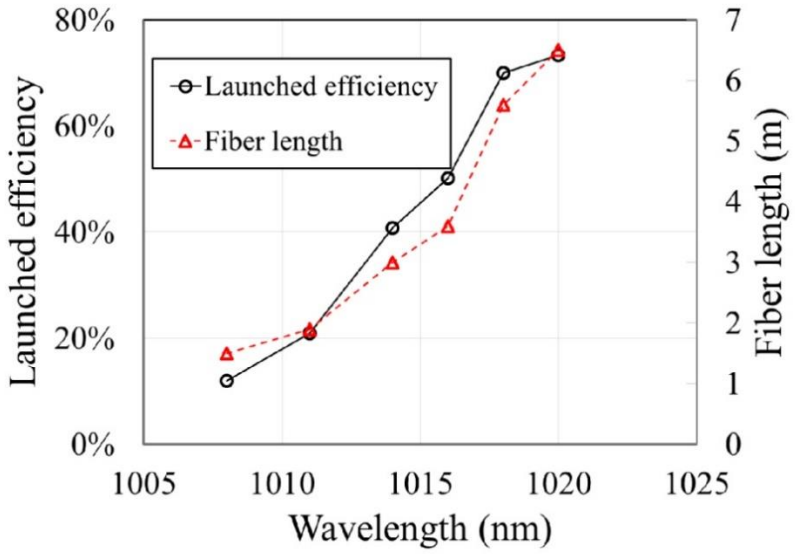

Fig. 5.4 Launched efficiency (black circle) and fiber length (red triangle) as a function of wavelength.

To further understand the mechanisms responsible for the poorer efficiency at shorter lasing wavelengths, we need to characterize slope efficiency with respect to both launched and absorbed pump powers at various inversion levels. It is hard to get an accurate measurement of the unabsorbed pump powers in order to determine the slope efficiency with respect to the absorbed pump powers in the case where a FBG is spliced to the Yb-doped fibers. We therefore decided to do the cut-back measurement in a free-running fiber laser without the FBG. Another ~6m Yb-doped LCF was used for the 1030nm fiber laser measurement. Two facets of the fiber were perpendicularly cleaved to serve as two reflectors at ~4% reflectivity thus the laser would naturally emit at ~1030nm. The experimental configuration is similar to that used in Chapter 2. The fiber was repeatedly cut back 40-50cm every time followed by laser efficiency test at each fiber length.

The slope efficiency with respect both to the launched and absorbed power of the 1030nm fiber laser versus the inverse of fiber length is plotted in Fig. 5.5. The free-running fiber laser measurements were done twice and both results are shown as the 1st measurement and the 2nd measurement. The inverse of fiber length serves as a good surrogate for the average inversion in case of constant round-trip loss. For comparison, the efficiency with respect to the launched pump power of the LCF-FBG fiber lasers is also presented. It can be clearly seen that the efficiency with respect to the launched pump power overlaps fairly well in all cases including the free-running fiber laser and the LCF-FBG fiber laser. The LCF-FBG fiber laser has a lower round-trip loss due to the much higher reflectivity of the FBG. The free-running fiber laser therefore operates at a much higher threshold gain and therefore a much higher average inversion for the same fiber

length. Despite the difference in inversion levels among the two types of fiber lasers, their efficiency with respect to the launched pump power versus inverse fiber length overlaps very well. This is a strong indication that the launched efficiency is primarily limited the poor pump absorption as a result of the shorter fiber length and is not related to the higher inversion. A further evidence is that the slope efficiency versus the absorbed pump power for the free-running laser at fiber length longer than 3m, i.e. 1/L<0.33, is between 92.4% to 93.5%, very close to the quantum limit of 94.7%. The average inversion of the free-running fiber laser with 3m-long fiber is estimated to be ~40% based on the round-trip loss and absorption/emission cross sections. This is higher than the average inversion of any of the fiber lasers with FBGs. The highest of which is ~40% for the LCF-FBG fiber laser with a lasing wavelength of 1008nm.

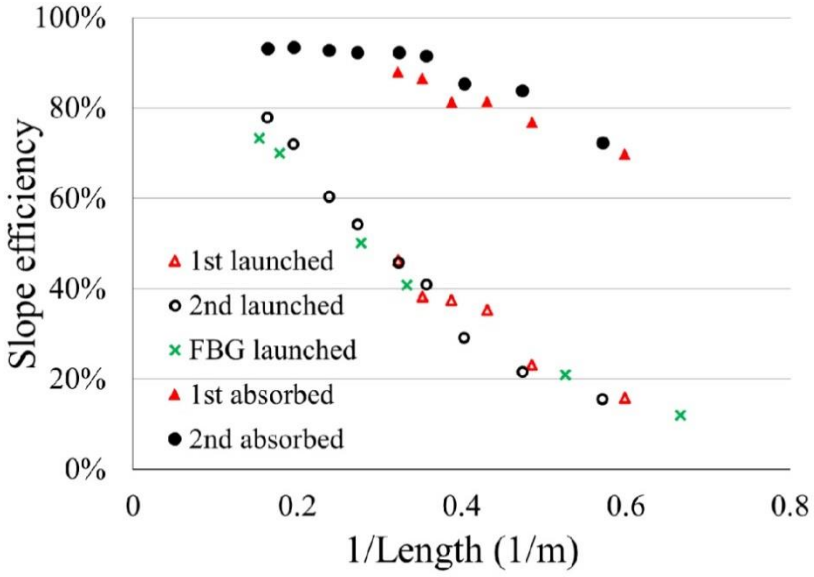

Fig. 5.5 Slope efficiency versus the inverse of the fiber length.

Another detail worth noting is that the absorbed efficiency of the free-running 1030nm fiber laser starts to decrease when the fiber is cut back to shorter than 3m, i.e. 1/L>0.33. This suggests that other loss mechanism is introduced at higher population inversion. This additional loss mechanism may be related to the cooperative luminescence as the characteristic green fluorescence indeed becomes more visible at shorter fiber length [107]. The difference between the measured absorbed efficiency and the quantum limited efficiency is plotted in Fig. 5.6 versus the estimated average inversion. A quadratic fit is expected if the cooperative up-conversion process is expected to be responsible for the deviation from the quantum limit. The data at higher inversion can indeed be reasonably fitted with a quadratic curve. At lower inversion, the measured data deviates from a quadratic fit. This poor fit at lower inversion may be due to the fact that other losses such as fiber background loss and measurement errors play a more significant role in this regime.

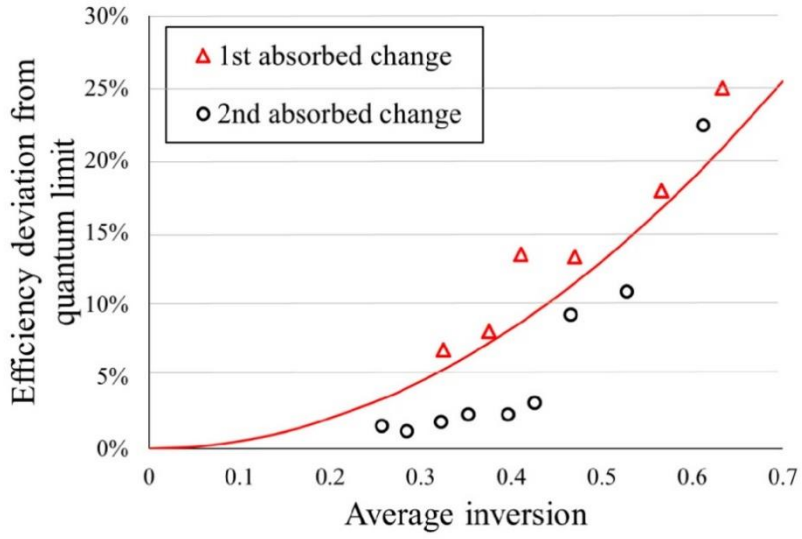

Fig. 5.6 Deviation of measured absorbed efficiency from quantum efficiency as a function of average inversion. Solid red line is the quadratic fit for the measured data.

Fig. 5.7 shows the net gain cross-section for the phosphosilicate host at various population inversion levels. This is obtained using the absorption and emission cross sections reported in [106]. The emission peaks of ytterbium-doped phosphosilicate fibers are at shorter wavelengths comparing to that of ytterbium-doped aluminosilicate fibers, due to a narrower Stark split [106]. Compared with aluminosilicate fiber, the phosphosilicate fiber has higher gain between 1000nm and 1020nm for the same inversion [106]. As it can have been seen that even with 20% population inversion, the net gain is positive in the 1000-1030nm range.

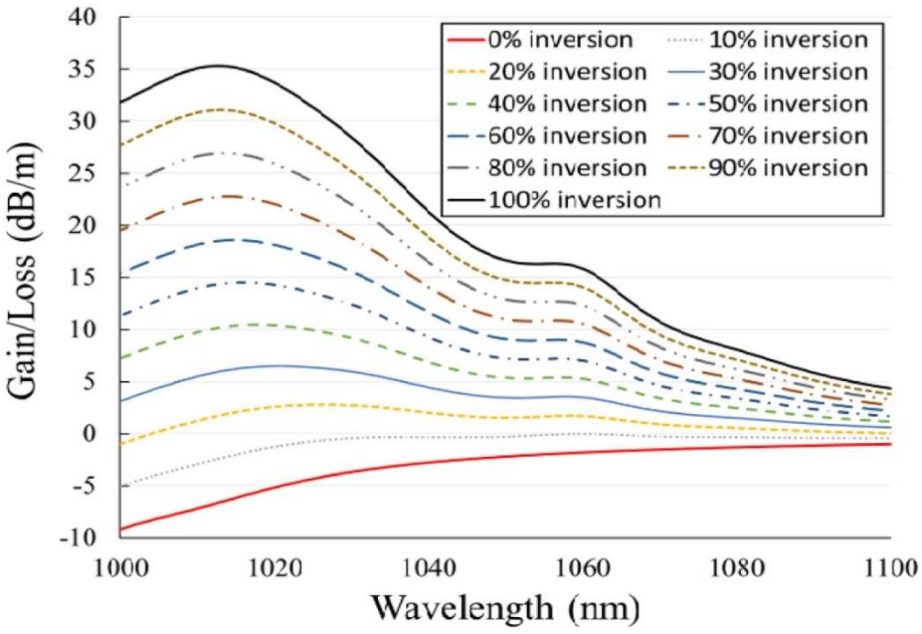

Fig. 5.7 Net gain in the phosphosilicate fiber.

5.4 Conclusion

In conclusion, we have demonstrated that ytterbium-doped phosphosilicate host is much superior for efficient lasing operation at wavelengths between 1008 and 1020nm comparing to conventional aluminoslilicate host. Highly efficient 1018nm fiber laser with 70% efficiency with respect to the launched pump power is demonstrated in a 50μm-core Yb-doped LCF with 420μm cladding diameter, demonstrating the low brightness pump required for such efficiency. This large cladding diameter will allow the use of much higher power, lower brightness pump diodes, which is essential for tandem pumping of single-mode fiber lasers at higher powers. The demonstrated 1018nm fiber laser has ~41dB ASE suppression, demonstrating the high stability of the laser. We have conducted further study to show that the poorer slope efficiency with respect to the launched pump power at shorter operating wavelengths is dominated by poorer pump absorption due to the shorter fiber length required to achieve stable operation. It is also found that there is an additional loss mechanism at higher population inversions, possibly due to the cooperative up-conversion.

The fiber lasers operate in multimode in this work due to the poor high-order-mode suppression in the LCF used. This is due to the lower refractive index of the ytterbium-doped glass, which modified the operation of the LCF [58]. Single-mode operation is possible with more optimized fibers such as those used in Chapter 2. Since single-mode operation is not necessary for tandem pumping, which is the focus of this work, we did not attempt it in this work. This work, however, demonstrates that efficient high-power single-mode ytterbium-doped fiber lasers at 1018nm is feasibly with single-mode photonic bandgap fibers or more optimized leakage channel fibers. These fiber lasers have a very

low quantum defect of 4.1% when pumped at 976nm, providing a path for the mitigation of thermal effects without the complexity of tandem pumping for multi-kilowatt fiber lasers.

CHAPTER SIX

CONCLUSIONS AND OUTLOOK

6.1 Conclusions

We have firstly conducted detailed studies on the new RE-LCF. The results confirm that the simulation based on infinite cladding is accurate for well confined modes with low waveguide losses. But for the highly leaky modes, the measured losses can be significantly lower than what are predicted by conventional simulation method at large coil diameters in the circular LCF. The measured loss, however, start to approach the simulation results at smaller coil diameters. The measured losses of the highly leak modes in the hexagonal LCF, on the other hand, are consistent with the simulation even at large coil diameters. HOM losses in excess of 20dB/m were measured. The results show that tight coiling can mitigate the effect of coherent reflection at outer boundary in fibers, possibly due to phase walk-off from the coiled cylindrical surface. The results from the rounded hexagonal fiber are even more startling. It suggests that a deviation from circular boundary can be very effective in mitigating the impact of the coherent reflection from outer boundary in fibers. The low-index polymer coating on this fiber does not seem to matter at all. This is strong evidence that the radiated powers from the core are reflected into the guided modes in the multimode pump waveguide. This is also a strong proof that the design concept of exploiting strong leakage losses of HOMs works even in double-clad fibers with a suitable design of fiber boundary.

In an all-solid photonic bandgap fiber, modes are only guided due to anti-resonance of cladding photonic crystal lattice. This provides strongly mode-dependent guidance, leading to very high differential mode losses. In addition, the all-solid nature of the fiber makes it easily spliced to other fibers. We have studied both theoretically and experimentally the possibility of further mode area scaling using all-solid photonic bandgap fibers. Our theoretical studies have shown that all-solid photonic bandgap fibers have the potential to provide significant higher order mode suppression. Our experimental studies have confirmed this to a large extent. We have demonstrated a record effective mode area of ~920μm^2 in all-solid photonic bandgap fibers with higher order mode content below −30dB. It was observed that mode instability can be initiated by very small amount of higher order modes when combining with thermal effects. Fibers with strong higher order mode suppression are critical for further power scaling of single mode fiber lasers to beyond kW levels.

Followed by the demonstration of passive AS-PBF. We then demonstrated a 50μm-core-diameter Yb-doped all-solid photonic bandgap fiber laser with a mode area ~1450μm^2 in a straight fiber and ~1020μm^2 when coiled at 50cm diameter. 75W output power has been generated with a diffraction-limited beam and an efficiency of 70% relative to the launched pump power. We have also experimentally confirmed that a robust single-mode regime exists near the high frequency edge of the bandgap. This work demonstrates the strong potential for mode area scaling of single-mode all-solid photonic bandgap fibers.

Using a novel design with multiple coupled smaller cores in the cladding, we have continued our effort in further mode area scaling, demonstrating a single-mode photonic

bandgap fiber with record effective mode area of ~2650μm^2. Detailed numeric studies have been conducted for multiple cladding designs. For the optimal designs, the simulated minimum higher-order-mode losses are well over two orders of magnitudes higher than that of fundamental mode when expressed in dBs. We have also experimentally validated one of the designs. M^2<1.08 across the transmission band was demonstrated.

Highly-efficient high-power fiber lasers operating at wavelength below 1020nm are critical for tandem-pumping in >10kW fiber lasers to provide high pump brightness and low thermal loading. Using an ytterbium-doped-phosphosilicate double-clad leakage-channel fiber with ~50μm core and ~420μm cladding, we have achieved ~70% optical-to-optical efficiency at 1018nm. The much larger cladding than those in previous reports demonstrates the much lower required pump brightness, a key for efficient kW operation. The demonstrated 1018nm fiber laser has ASE suppression of ~41dB. Limiting factors to efficiency are also systematically studied.

6.2 Outlook

To date, LMA fiber is the most effective way to mitigate nonlinear effects. Mode instability has become the major bottleneck for pushing the output power even higher. Therefore, it is of primary importance to overcome the LMA fiber's tendency to support multiple modes. The research narrated in this dissertation has provided a basis for tackling the mode instability issue. Developing low quantum defect high power fiber lasers with better mode control capability is of great interest. By incorporating PBF into 1018nm fiber laser system, it is possible to achieve single-transverse-mode output with relatively high

efficiency and lower TMI. The scope of this dissertation is limited within Yb-doped system. However, it is also important to extend the coverage of high power fiber lasers to other wavelength regime such as ~1.55μm and ~2μm. The issue for constructing Er-doped and Tm-doped system can be more challenging. The research of these fiber lasers is expected to be carried out soon.

APPENDICES

Appendix A

PUBLICATION LIST

Refereed Journal Publications

1. G. Gu, F. Kong, T.W. Hawkins, P. Foy, K. Wei, B. Samson, and L. Dong, "Impact of fiber outer boundaries on leaky mode losses in leakage channel fibers," Optics Express 21, 24039-24048 (2013).
2. F. Kong, G. Gu, T.W. Hawkins, J. Parsons, M. Jones, C. Dunn, M.T. Kalichevsky-Dong, K. Wei, B. Samson, and L. Dong, "Flat-top mode from a 50 μm-core Yb-doped leakage channel fiber," Optics Express 21, 32371-32376 (2013).
3. G. Gu, F. Kong, T. Hawkins, J. Parsons, M. Jones, C. Dunn, M.T. Kalichevsky-Dong, K. Saitoh, and L. Dong, "Ytterbium-doped large-mode-area all-solid photonic bandgap fiber lasers," Optics Express 22, 13962-13968(2014).
4. F. Kong, G. Gu, T.W. Hawkins, J. Parsons, M. Jones, C. Dunn, M.T. Kalichevsky-Dong, S.P. Palese, E. Cheung, and L. Dong, "Quantitative mode quality characterization of fibers with extremely large mode areas by matched white-light interferometry," Optics Express 22, 14657- 14665 (2014).
5. M. Steinke, H. Tünnermann, J. Neumann, D. Kracht, B. Samson, G. Gu, L. Dong, and P. Wessels, "TEM00 mode content measurements on a passive leakage channel fiber," Optics Letters, 40, 383-386(2015).
6. F. Kong, G. Gu, T.W. Hawkins, J. Parsons, M. Jones, C. Dunn, M.T. Kalichevsky-Dong, B. Pulford, I. Dajani, K. Saitoh, S.P. Palese, E. Cheung, and L. Dong, "Polarizing ytterbium-doped all-solid photonic bandgap fiber with ~1150μm2 effective mode area," Optics Express 23, 4307- 4312 (2015).
7. G. Gu, F. Kong, T.W. Hawkins, M. Jones, and L. Dong, "Extendin Mode Areas of Single-mode All-solid Photonic Bandgap Fibers," Optics Express 23, 9147-9156 (2015).

8. G. Gu, Z. Liu, F. Kong, H. Tam, R.K. Shori and L. Dong, “Highly efficient ytterbium-doped phosphosilicate fiber lasers operating below 1020nm,” Opt. Express 23(14), 17693-17700 (2015).
9. L. Dong, F. Kong, G. Gu, T. W. Hawkins, M. Jones, J. Parsons, M. T. Kalichevsky-Dong, K. Saitoh, B. Pulford, and I. Dajani, "Large-Mode-Area All-Solid Photonic Bandgap Fibers for the Mitigation of Optical Nonlinearities," IEEE J. Sel. Top. Quantum Electron. 22, (2016)

Conference Proceedings (Reviewed)

1. L. Dong, K. Saitoh, F. Kong, P. Foy, T.W. Hawkins, D. Mcclane, G. Gu, and Y. Dong, “All-Solid Photonic Bandgap Fibers for High Power Lasers," SPIE Security and Defense, paper 8547-18, invited paper, September 2012, Edinburg, Scotland.
2. L. Dong, K. Saitoh, F. Kong, T.W. Hawkins, G. Gu, and Y. Dong, “Advanced Optical Fibers and Their Applications in Fiber Lasers," Frontier in Optics, paper FTh3C.4, invited paper, October 2012, Rochester, New York.
3. L. Dong, K. Saitoh, F. Kong, T. Hawkins, D. Mcclane and G.C. Gu, “Advanced Optical Fibers and Their Applications in Fiber Lasers,” Photonics Global Conference, paper 3-1F-1, invited paper, December 2012 in Singapore.
4. L. Dong, K. Saitoh, F. Kong, T. Hawkins, D. Mcclane, and G.C. Gu, “Robust Single-mode All Solid Photonic Bandgap Fibers with Core Diameter of 50μm,” PhotonicsWest, paper 8601-64, 2013.
5. F. Kong, K. Saitoh, D. Mcclane, T.W. Hawkins, P. Foy, G.C. Gu and L. Dong, “All-solid photonic bandgap fiber with record mode area,” Optical Communications Conference, paper OTh1J2, 2013.
6. G. Gu, F. Kong, T.W. Hawkins, L. Dong, K. Wei, and B. Samson “Mode-dependent Losses in 50micron Core Leakage Channel Fibers,” DEPS Solid State and Diode Laser Review, paper 13-SSDLTR 004, 2013.

7. L. Dong, F. Kong, T. Hawkins; G. Gu, P. Foy, K. Saitoh, K. Wei; B. Samson, "Large-mode-area Fibers Enabled by Significant Differential Mode Losses," Workshop on Specialty Optical Fibers, invited talk, Sigtuna Sweden, August 2013.
8. G. Gu, F. Kong, T.W. Hawkins, P. Foy, K. Wei, B. Samson, and L. Dong, "Measurements of Mode Losses in ~50μm Core Resonantly Enhanced Leakage Channel Fibers," Advanced Solid State Lasers, paper AM4A.04, Paris, October 2013.
9. F. Kong, G. Gu, T.W. Hawkins, J. Parsons, M. Jones, C. Dunn, M.T. Kalichevsky-Dong, K. Wei, B. Samson, and L. Dong, "Flat-top Beam from a 50μm-Core Yb-doped Leakage Channel Fiber," Optical Communications Conference, paper Tu3K.5, March 2014.
10. F. Kong, G. Gu, T. Hawkins, J. Parsons, M. Jones, C. Dunn, M.Kalichevsky-Dong and L. Dong, "50μm-Core Yb-doped Leakage Channel Fiber with Flattened Mode," Sixteenth Annual Directed Energy Symposium, paper 13-Symp-064, March 2014.
11. F. Kong, G. Gu, T.W. Hawkins, J. Parsons, M. Jones, C. Dunn, M.T. Kalichevsky-Dong, K. Wei, B. Samson, and L. Dong, "50μm-core Yb-doped leakage channel fiber with flattened mode," of SPIE Defense and Security. Paper 9081-14, May 2014.
12. G. Gu; F. Kong; T.W. Hawkings; J. Parsons; M. Jones; C. Dunn; M.T. Kalichevsky-Dong; K. Saitoh; L. Dong, "High power, large core ytterbium-doped photonic bandgap fiber laser," DEPS Advanced High Power Lasers, paper 14-SSDLTR-009, May 2014.
13. G. Gu; F. Kong; T. Hawkings; J. Parsons; M. Jones; C. Dunn; M.T. Kalichevsky-Dong; K. Saitoh; L. Dong, " Yb-Doped Photonic Bandgap Fiber Lasers with Record Core Diameter," CLEO, paper SF1N.2, June 2014.
14. F. Kong, G. Gu, T.W. Hawkins, J. Parsons, M. Jones, C. Dunn, M.T. Kalichevsky-Dong, K. Wei, B. Samson, and L. Dong, "80W Flat-top Beam from an Yb-doped

Leakage Channel Fiber," International Photonics and OptoElectronics (POEM), paper FF3D.3 June 2014.

15. G. Gu, F. Kong, T. Hawkins, J. Parsons, M. Jones, C. Dunn, M.T. Kalichevsky-Dong, K. Saitoh, and L. Dong, "Yb-Doped All-Solid Photonic Bandgap Fiber Lasers," International Photonics and OptoElectronics (POEM), paper FTh4F.5 June 2014.
16. G. Gu, F. Kong, T. Hawkins, J. Parsons, M. Jones, C. Dunn, M.T. Kalichevsky-Dong, K. Saitoh, and L. Dong, "Large-Mode-Area Yb-Doped Photonic Bandgap Fiber Laser," Advanced Photonics Congress, paper SoTu4B.3, August 2014.
17. F. Kong, G. Gu, T.W. Hawkins, J. Parsons, M. Jones, C. Dunn, M.T. Kalichevsky-Dong, S.P. Palese, E. Cheung, and L. Dong, "Quantitative Mode Quality Characterization in a Leakage Channel Fiber with 100 μm Core Diameter," Advanced Photonics Congress, paper SoW2B.5, August 2014.
18. L. Dong, F. Kong, G. Gu, T.W. Hawkins, J. Parsons, M. Jones, C. Dunn, M.T. Kalichevsky-Dong, K. Saitoh, B. Pulford, and I. Dajani, "Large mode area Yb-doped photonic bandgap fiber lasers," SPIE PhotonicsWest, invited talk, paper 9344-1, San Francisco, February 2015.
19. F. Kong, G. Gu, T.W. Hawkins, J. Parsons, M. Jones, C.D. Dunn, M.T. Kalichevsky-Dong, B. Pulford, I. Dajani, K. Saitoh, L. Dong, "Polarizing 50μm core Yb-doped photonic bandgap fiber," SPIE PhotonicsWest, paper 9344-2, San Francisco, February 2015.
20. B. Pulford, I. Dajani, T. Ehrenreich, R.H. Holten, C.L. Vergien, N. Naderi, C. Mart, G. Gu, F. Kong, T.W. Hawkins, and L. Dong, "High-power narrow-linewidth large mode area photonic bandgap fiber amplifier," SPIE PhotonicsWest, paper 9344-5, San Francisco, February 2015.
21. L. Dong, F. Kong, G. Gu, T.W. Hawkins, J. Parsons, M. Jones, C. Dunn, M.T. Kalichevsky-Dong, K. Saitoh, B. Pulford, and I. Dajani, "High-Power All-solid Photonic Bandgap Fiber Lasers," 17th Annual Directed Energy Symposium, Anaheim, CA, March 2015.

22. G. Gu, F. Kong, T.W. Hawkins, M. Jones, and L. Dong, “Large Mode Area, All-Solid Photonic Bandgap Fiber with Resonant Cladding Cores,” 17th Annual Directed Energy Symposium, Anaheim, CA, March 2015.
23. G. Gu; F. Kong, T. Hawkins, M. Jones, and L Dong, “Multiple Cladding-Resonance All-Solid Photonic Bandgap Fibers with Large Mode Area,” CLEO, SM2L.1, San Jose, CA, May 10-15 2015.
24. L. Dong, F. Kong, G. Gu, T. Hawkins, M. Jones, J. Parsons, M. Kalichevsky-Dong, K. Saitoh, B. Pulford, and I. Dajani, "Challenges for Further Power Scaling of Single-Mode Fiber Lasers," in Advanced Solid State Lasers, OSA Technical Digest (online) (Optical Society of America, 2015), paper AM4A.1.
25. L. Dong, F. Kong, G. Gu, T. Hawkins, M. Jones, J. Parsons, M. Kalichevsky-Dong, K. Saitoh, B. Pulford, and I. Dajani, "Large-Mode-Area All-Solid Photonic Bandgap Fibers for High Power Fiber Lasers," in Frontiers in Optics 2015, OSA Technical Digest (online) (Optical Society of America, 2015), paper FM3G.1.
26. G. Gu, Z. Liu, f. Kong, H. Y. Tam, R. Shori, and L. Dong, "High-power Efficient Yb-doped Fiber Laser with Low Quantum Defect," in Workshop on Specialty Optical Fibers and Their Applications, OSA Technical Digest (online) (Optical Society of America, 2015), paper WT2A.4.
27. Guancheng Gu; Zhengyong Liu; Fanting Kong; Hwayaw Tam; Ramesh K. Shore; Liang Dong; “Efficient ytterbium-doped phosphosilicate double-clad leakage-channel-fiber laser at 1008-1020nm”. Proc. SPIE 9728, Fiber Lasers XIII: Technology, Systems, and Applications, 97282Q (March 11, 2016); doi:10.1117/12.2200999.

Invited/Keynote speech at international conferences

1. L. Dong, K. Saitoh, F. Kong, P. Foy, T.W. Hawkins, D. Mcclane, G. Gu, and Y. Dong, “All-Solid Photonic Bandgap Fibers for High Power Lasers," SPIE Security and Defense, paper 8547-18, invited paper, September 2012, Edinburg, Scotland.

2. L. Dong, K. Saitoh, F. Kong, T.W. Hawkins, G. Gu, and Y. Dong, “Advanced Optical Fibers and Their Applications in Fiber Lasers," Frontier in Optics, paper FTh3C.4, invited paper, October 2012, Rochester, New York.
3. L. Dong, K. Saitoh, F. Kong, T. Hawkins, D. Mcclane and G.C. Gu, “Advanced Optical Fibers and Their Applications in Fiber Lasers,” Photonics Global Conference, paper 3-1F-1, invited paper, December 2012 in Singapore.
4. L. Dong, F. Kong, T. Hawkins; G. Gu, P. Foy, K. Saitoh, K. Wei; B. Samson, “Large-mode-area Fibers Enabled by Significant Differential Mode Losses,” Workshop on Specialty Optical Fibers, invited talk, Sigtuna Sweden, August 2013.
5. L. Dong, F. Kong, G. Gu, T.W. Hawkins, J. Parsons, M. Jones, C. Dunn, M.T. Kalichevsky-Dong, K. Saitoh, B. Pulford, and I. Dajani, “Large mode area Yb-doped photonic bandgap fiber lasers,” SPIE PhotonicsWest, invited talk, paper 9344-1, San Francisco, February 2015.

Reference

1. F. P. Kapron, D. B. Keck, and R. D. Maurer, "Radiation losses in glass optical waveguides," Appl. Phys. Lett. **17**, 423–425 (1970).
2. F. P. Kapron and D. B. Keck, "Pulse Transmission Through a Dielectric Optical Waveguide," Appl. Opt. **10**, 1519 (1971).
3. E. Snitzer, "Proposed fiber cavities for optical masers," J. Appl. Phys. **32**, 36–39 (1961).
4. E. Snitzer, "Optical maser action of Nd+3 in a barium crown glass," Phys. Rev. Lett. **7**, 444–446 (1961).
5. J. Stone and C. A. Burrus, "Neodymium-doped silica lasers in end-pumped fiber geometry," Appl. Phys. Lett. **23**, 388–389 (1973).
6. C. J. Koester and E. Snitzer, "Amplification in a Fiber Laser," Appl. Opt. **3**, 1182 (1964).
7. S. B. Poole, D. N. Payne, and M. E. Fermann, "Fabrication of low-loss optical fibres containing rare-earth ions," Electron. Lett. **21**, 737 (1985).
8. R. J. Mears, L. Reekie, S. B. Poole, and D. N. Payne, "Neodymium-doped silica single-mode fibre lasers," Electron. Lett. **21**, 738–740 (1985).
9. R. Mears, L. Reekie, I. Jauncey, and D. Payne, "Low-noise erbium-doped fibre amplifier operating at 1.54μm," Electron. Lett. **23**, 1026–1028 (1987).
10. M. L. Osowski, W. Hu, R. M. Lammert, S. W. Oh, P. T. Rudy, T. Stakelon, L. Vaissie, and J. E. Ungar, "Advances in high-brightness semiconductor lasers," **6952**, 695208–695208–8 (2008).
11. E. Snitzer, H. Po, F. Hakimi, R. Tumminelli, and B. C. McCollum, "Double clad, offset core Nd fiber laser," Opt. Fiber Sensors **2**, PD5 (1988).
12. https://en.wikipedia.org/wiki/Double-clad_fiber.
13. E. Stiles, "New developments in IPG fiber laser technologye," in *Proceedings of the 5th International Workshop on Fiber Lasers* (2009).
14. V. Dominic, S. MacCormack, R. Waarts, S. Sanders, S. Bicknese, R. Dohle, E. Wolak, P. S. Yeh, and E. Zucker, "110 W fiber laser," Lasers Electro-Optics, 1999.

CLEO’99. Summ. Pap. Present. Conf. CPD11–1 (n.d.).

15. Y. Jeong, J. K. Sahu, D. N. Payne, and J. Nilsson, "Ytterbium-doped large-core fibre laser with 1 kW of continuous-wave output power," Electron. Lett. **40**, 470 (2004).
16. F. Roeser, C. Jauregui, J. Limpert, and A. Tünnermann, "94 W 980 nm high brightness Yb-doped fiber laser," Opt. Express **16**, 17310 (2008).
17. F. Röser, J. Rothhard, B. Ortac, A. Liem, O. Schmidt, T. Schreiber, J. Limpert, and A. Tünnermann, "131 W 220 fs fiber laser system," Opt. Lett. **30**, 2754–2756 (2005).
18. T. Eidam, S. Hanf, E. Seise, T. V Andersen, T. Gabler, C. Wirth, T. Schreiber, J. Limpert, and A. Tünnermann, "Femtosecond fiber CPA system emitting 830 W average output power.," Opt. Lett. **35**, 94–96 (2010).
19. C. Jauregui, J. Limpert, and A. Tünnermann, "High-power fibre lasers," Nat. Photonics **7**, 861–867 (2013).
20. P. Sprangle, B. Hafizi, A. Ting, and R. Fischer, "High-power lasers for directed-energy applications," Appl. Opt. **54**, F201 (2015).
21. T. Katsouleas, "Accelerator physics: electrons hang ten on laser wake.," Nature **431**, 515–516 (2004).
22. J. J. Macklin, J. D. Kmetec, and C. L. Gordon, "High-order harmonic generation using intense femtosecond pulses," Phys. Rev. Lett. **70**, 766–769 (1993).
23. M. Pitkin, S. Reid, S. Rowan, and J. Hough, "Gravitational wave detection by Interferometry (Ground and Space)," Living Rev. Relativ. **14**, (2011).
24. https://en.wikipedia.org/wiki/Laser_Weapon_System.
25. D. J. Richardson, J. Nilsson, and W. A. Clarkson, "High power fiber lasers: current status and future perspectives," J. Opt. Soc. Am. B-optical Phys. **27**, B63–B92 (2010).
26. A. Kobyakov, M. Sauer, and D. Chowdhury, "Stimulated Brillouin scattering in optical fibers," Adv. Opt. Photonics **2**, 1 (2010).
27. M.-J. Li, X. Chen, J. Wang, S. Gray, A. Liu, J. a Demeritt, a B. Ruffin, A. M. Crowley, D. T. Walton, L. A. Zenteno, and A. Boh, "Al/Ge co-doped large mode area fiber with high SBS threshold.," Opt. Express **15**, 8290–9 (2007).

28. J. M. Fini, M. D. Mermelstein, M. F. Yan, R. T. Bise, a D. Yablon, P. W. Wisk, and M. J. Andrejco, "Distributed suppression of stimulated Raman scattering in an Yb-doped filter-fiber amplifier.," Opt. Lett. **31**, 2550–2552 (2006).
29. R. H. Stolen and C. Lin, "Self-phase-modulation in silica optical fibers," Phys. Rev. A **17**, 1448–1453 (1978).
30. R. L. Farrow, D. a V Kliner, G. R. Hadley, and A. V Smith, "Peak-power limits on fiber amplifiers imposed by self-focusing.," Opt. Lett. **31**, 3423–3425 (2006).
31. D. N. Schimpf, T. Eidam, E. Seise, S. Hädrich, J. Limpert, and A. Tünnermann, "Circular versus linear polarization in laser-amplifiers with Kerr-nonlinearity.," Opt. Express **17**, 18774–18781 (2009).
32. H.-J. Otto, F. Stutzki, F. Jansen, T. Eidam, C. Jauregui, J. Limpert, and A. Tünnermann, "Temporal dynamics of mode instabilities in high-power fiber lasers and amplifiers," Opt. Express **20**, 15710 (2012).
33. A. V Smith and J. J. Smith, "Mode instability in high power fiber amplifiers.," Opt. Express **19**, 10180–10192 (2011).
34. T. Eidam, C. Wirth, C. Jauregui, F. Stutzki, F. Jansen, H. Otto, O. Schmidt, T. Schreiber, J. Limpert, and A. Tünnermann, "Experimental observations of the threshold-like onset of mode instabilities in high power fiber amplifiers.," Opt. Express **19**, 13218–13224 (2011).
35. K. Brar, M. Savage-leuchs, J. Henrie, S. Courtney, C. Dilley, and R. Afzal, "Threshold power and fiber degradation induced modal instabilities in high power fiber amplifiers based on large mode area fibers," SPIE Photonics West 2014-LASE Lasers Sources **8961**, 1–9 (2014).
36. L. Dong, "Stimulated thermal Rayleigh scattering in optical fibers," Opt. Express **21**, 2642 (2013).
37. C. Jauregui, T. Eidam, H. Otto, F. Stutzki, F. Jansen, J. Limpert, and A. Tünnermann, "Temperature-induced index gratings and their impact on mode instabilities in high-power fiber laser systems," Opt. Express **20**, 440 (2012).
38. C. Jauregui, T. Eidam, J. Limpert, and A. Tünnermann, "The impact of modal

interference on the beam quality of high-power fiber amplifiers.," Opt. Express **19**, 3258–3271 (2011).

39. F. Kong, K. Saitoh, D. Mcclane, T. Hawkins, P. Foy, G. Gu, and L. Dong, "Mode area scaling with all-solid photonic bandgap fibers.," Opt. Express **20**, 26363–72 (2012).
40. E. M. Dianov, M. E. Likhachev, and S. Février, "Solid-core photonic bandgap fibers for high-power fiber lasers," IEEE J. Sel. Top. Quantum Electron. **15**, 20–29 (2009).
41. D. Taverner, D. J. Richardson, L. Dong, J. E. Caplen, K. Williams, and R. V Penty, "158 μJ pulses from a single-transverse-mode, large-mode-area erbium-doped fiber amplifier," Opt. Lett. **22**, 378–380 (1997).
42. W. Xu, Z. Lin, M. Wang, S. Feng, L. Zhang, Q. Zhou, D. Chen, L. Zhang, S. Wang, C. Yu, and L. Hu, "50 μm core diameter Yb3+/Al3+/F− codoped silica fiber with M^2<11 beam quality," Opt. Lett. **41**, 504 (2016).
43. V. Petit, R. P. Tumminelli, J. D. Minelly, and V. Khitrov, " Extremely low NA Yb doped preforms (<0.03) fabricated by MCVD ," in (2016), Vol. 9728, p. 97282R–97282R–7.
44. D. Jain, Y. Jung, P. Barua, S. Alam, and J. K. Sahu, "Demonstration of ultra-low NA rare-earth doped step index fiber for applications in high power fiber lasers," Opt. Express **23**, 5200–5203 (2015).
45. V. Khitrov, J. D. Minelly, R. Tumminelli, V. Petit, and E. S. Pooler, "3kW single-mode direct diode-pumped fiber laser," in *SPIE LASE* (2014), p. 89610V–89610V.
46. C. Hupel, S. Kuhn, S. Hein, N. Haarlammert, J. Nold, F. Beier, B. Sattler, T. Schreiber, R. Eberhardt, and A. Tünnermann, "MCVD Based Fabrication of Low-NA Fibers for High Power Fiber Laser Application," 5–7 (2015).
47. P. S. J. Russell, "Photonic-crystal fibers," J. Light. Technol. **24**, 4729–4749 (2006).
48. T. a Birks, J. C. Knight, and P. S. Russell, "Endlessly single-mode photonic crystal fiber.," Opt. Lett. **22**, 961–963 (1997).
49. T. Schreiber, J. Limpert, S. Nolte, H. Zellmer, A. Tunnermann, R. Iliew, F. Lederer, J. Broeng, G. Vienne, A. Petersson, and C. Jakobsen, "High-power air-clad large-

mode-area photonic crystal fiber laser," in *Conference on Lasers and Electro-Optics Europe - Technical Digest* (2003), p. 656.

50. W. J. Wadsworth, R. M. Percival, G. Bouwmans, J. C. Knight, and P. S. J. Russel, "High power air-clad photonic crystal fibre laser," Opt. Express **11**, 48–53 (2003).
51. P. S. J. R. and J. A. W.J. Wadsworth, J.C. Knight, W.H. Reeves, "Yb3+-doped photonic crystal fibre laser," Electron. Lett. **36**, 1998–2000 (2000).
52. R. F. Cregan, J. C. Knight, P. S. J. Russell, and P. J. Roberts, "Distribution of spontaneous emission from an Er^{3+}-doped\nphotonic crystal fiber," J. Light. Technol. **17**, 2138–2141 (1999).
53. J. Limpert, O. Schmidt, J. Rothhardt, F. Röser, T. Schreiber, a Tünnermann, S. Ermeneux, P. Yvernault, and F. Salin, "Extended single-mode photonic crystal fiber lasers.," Opt. Express **14**, 2715–2720 (2006).
54. J. Fini, "Design of solid and microstructure fibers for suppression of higher-order modes.," Opt. Express **13**, 3477–3490 (2005).
55. M. C. Swan, L. Chi-Hung, G. Doug, J. Nick, T. Kanishka, and G. Almantas, "33μm core effectively single-mode Chirally-Coupled-Core fiber laser at 1064nm," OFC/NFOEC 2008 - 2008 Conf. Opt. Fiber Commun. Fiber Opt. Eng. Conf. 22–24 (2008).
56. L. Dong, H. A. Mckay, A. Marcinkevicius, L. Fu, J. Li, B. K. Thomas, and M. E. Fermann, "Extending Effective Area of Fundamental Mode in Optical Fibers," J. Light. Technol. **27**, 1565–1570 (2009).
57. L. Dong, H. A. McKay, L. Fu, M. Ohta, A. Marcinkevicius, S. Suzuki, and M. E. Fermann, "Ytterbium-doped all glass leakage channel fibers with highly fluorine-doped silica pump cladding.," Opt. Express **17**, 8962–8969 (2009).
58. F. Kong, G. Gu, T. W. Hawkins, J. Parsons, M. Jones, C. Dunn, M. T. Kalichevsky-Dong, K. Wei, B. Samson, and L. Dong, "Flat-top beam from a 50μm-core Yb-doped leakage channel fiber," Conf. Opt. Fiber Commun. Tech. Dig. Ser. **21**, 32371–6 (2014).
59. A. Isomäki and O. G. Okhotnikov, "Femtosecond soliton mode-locked laser based

on ytterbium-doped photonic bandgap fiber," Conf. Proc. - Lasers Electro-Optics Soc. Annu. Meet. **14**, 394–395 (2007).

60. A. Shirakawa, H. Maruyama, K. Ueda, C. B. Olausson, J. K. Lyngsø, and J. Broeng, "High-power Yb-doped photonic bandgap fiber amplifier at 1150-1200 nm.," Opt. Express **17**, 447–454 (2009).
61. B. Ward, "Solid-core photonic bandgap fibers for cladding-pumped Raman amplification.," Opt. Express **19**, 11852–66 (2011).
62. M. Kashiwagi, K. Saitoh, K. Takenaga, S. Tanigawa, S. Matsuo, and M. Fujimaki, "Effectively single-mode all-solid photonic bandgap fiber with large effective area and low bending loss for compact high-power all-fiber lasers," Opt. Express **20**, 15061 (2012).
63. S. Saitoh, K. Saitoh, M. Kashiwagi, S. Matsuo, and L. Dong, "Design optimization of large-mode-area all-solid photonic bandgap fibers for high-power laser applications," J. Light. Technol. **32**, 440–449 (2014).
64. F. Kong, K. Saitoh, D. Mcclane, T. Hawkins, P. Foy, G. Gu, and L. Dong, "Mode area scaling with all-solid photonic bandgap fibers.," Opt. Express **20**, 26363–72 (2012).
65. L. Dong, X. Peng, and J. Li, "Leakage channel optical fibers with large effective area," J. Opt. Soc. Am. B **24**, 1689 (2007).
66. M. Kashiwagi, K. Saitoh, K. Takenaga, S. Tanigawa, S. Matsuo, and M. Fujimaki, "Low bending loss and effectively single-mode all-solid photonic bandgap fiber with an effective area of 650μm^2," Opt. Lett. **37**, 1292 (2012).
67. K. Saitoh, S. Varshney, K. Sasaki, L. Rosa, M. Pal, M. C. Paul, D. Ghosh, S. K. Bhadra, and M. Koshiba, "Limitation on effective area of bent large-mode-area leakage channel fibers," J. Light. Technol. **29**, 2609–2615 (2011).
68. L. Dong, T. W. Wu, H. A. McKay, L. Fu, J. Li, and H. G. Winful, "All-glass large-core leakage channel fibers," IEEE J. Sel. Top. Quantum Electron. **15**, 47–53 (2009).
69. R. a Barankov, K. Wei, B. Samson, and S. Ramachandran, "Resonant bend loss in leakage channel fibers.," Opt. Lett. **37**, 3147–9 (2012).

70. R. Barankov, K. Wei, B. Samson, and S. Ramachandran, "Anomalous Bend Loss in Large-Mode Area Leakage Channel Fibers," in *Conference on Lasers and Electro-Optics 2012* (OSA, 2012), Vol. 37, p. CM1N.3.
71. J. W. Nicholson, a D. Yablon, S. Ramachandran, and S. Ghalmi, "Spatially and spectrally resolved imaging of modal content in large-mode-area fibers.," Opt. Express **16**, 7233–7243 (2008).
72. Y. Jeong, J. Sahu, D. Payne, and J. Nilsson, "Ytterbium-doped large-core fiber laser with 1.36 kW continuous-wave output power.," Opt. Express **12**, 6088–6092 (2004).
73. T. Murao, K. Saitoh, and M. Koshiba, "Detailed theoretical investigation of bending properties in solid-core photonic bandgap fibers.," Opt. Express **17**, 7615–29 (2009).
74. K. Saitoh and M. Koshiba, "Full-vectorial imaginary-distance beam propagation method based on a finite element scheme: application to photonic crystal fibers," IEEE J. Quantum Electron. **38**, 927–933 (2002).
75. K. Saitoh and M. Koshiba, "Full-vectorial finite element beam propagation method with perfectly matched layers for anisotropic optical waveguides," J. Light. Technol. **19**, 405–413 (2001).
76. L. Dong, F. Kong, G. Gu, T. W. Hawkins, M. Jones, J. Parsons, M. T. Kalichevsky-Dong, K. Saitoh, B. Pulford, and I. Dajani, "Large-Mode-Area All-Solid Photonic Bandgap Fibers for the Mitigation of Optical Nonlinearities," IEEE J. Sel. Top. Quantum Electron. **22**, (2016).
77. F. Kong, G. Gu, T. W. Hawkins, J. Parsons, M. Jones, C. Dunn, M. T. Kalichevsky-Dong, B. Pulford, I. Dajani, K. Saitoh, S. P. Palese, E. Cheung, and L. Dong, "Polarizing ytterbium-doped all-solid photonic bandgap fiber with ~1150μm^2 effective mode area," Opt. Express **23**, 4307–4312 (2015).
78. O. N. Egorova, S. L. Semjonov, A. F. Kosolapov, A. N. Denisov, A. D. Pryamikov, D. A. Gaponov, A. S. Biriukov, E. M. Dianov, M. Y. Salganskii, V. F. Khopin, M. V Yashkov, A. N. Gurianov, and D. V Kuksenkov, "Single-mode all-silica photonic bandgap fiber with 20μm mode-field diameter.," Opt. Express **16**, 11735–40 (2008).
79. K. Saitoh, T. Murao, L. Rosa, and M. Koshiba, "Effective area limit of large-mode-

area solid-core photonic bandgap fibers for fiber laser applications," Opt. Fiber Technol. **16**, 409–418 (2010).

80. a Argyros, T. Birks, S. Leon-Saval, C. M. B. Cordeiro, and P. St J Russell, "Guidance properties of low-contrast photonic bandgap fibres.," Opt. Express **13**, 2503–2511 (2005).
81. T. a Birks, G. J. Pearce, and D. M. Bird, "Approximate band structure calculation for photonic bandgap fibres.," Opt. Express **14**, 9483–9490 (2006).
82. a Argyros, T. Birks, S. Leon-Saval, C. M. Cordeiro, F. Luan, and P. S. J. Russell, "Photonic bandgap with an index step of one percent.," Opt. Express **13**, 309–314 (2005).
83. J. Lægsgaard, "Gap formation and guided modes in photonic bandgap fibres with high-index rods," J. Opt. A Pure Appl. Opt. **6**, 798–804 (2004).
84. L. Dong, "A vector boundary matching technique for efficient and accurate determination of photonic bandgaps in photonic bandgap fibers.," Opt. Express **19**, 12582–93 (2011).
85. F. Luan, A. George, T. Hedley, G. Pearce, D. Bird, J. Knight, and P. Russell, "All-solid photonic bandgap fiber," Opt. Lett. **29**, 2369 (2004).
86. F. Jansen, F. Stutzki, H.-J. Otto, M. Baumgartl, C. Jauregui, J. Limpert, and A. Tünnermann, "The influence of index-depressions in core-pumped Yb-doped large pitch fibers.," Opt. Express **18**, 26834–26842 (2010).
87. M. J. F. Digonnet, H. K. Kim, G. S. Kino, and S. Fan, "Understanding air-core photonic-bandgap fibers: Analogy to conventional fibers," J. Light. Technol. **23**, 4169–4177 (2005).
88. F. Stutzki, F. Jansen, T. Eidam, A. Steinmetz, C. Jauregui, J. Limpert, and A. Tünnermann, "High average power large-pitch fiber amplifier with robust single-mode operation.," Opt. Lett. **36**, 689–691 (2011).
89. T. Schreiber, J. Limpert, S. Nolte, H. Zellmer, A. Tunnermann, R. Iliew, F. Lederer, J. Broeng, G. Vienne, A. Petersson, and C. Jakobsen, "High-power air-clad large-mode-area photonic crystal fiber laser," Conf. Lasers Electro-Optics Eur. - Tech.

Dig. **11**, 656 (2003).

90. S. Saitoh, K. Saitoh, M. Kashiwagi, S. Matsuo, and L. Dong, "Design Optimization of Large-Mode-Area All-Solid Photonic Bandgap Fibers for High-Power Laser Applications," J. Light. Technol. **32**, 440–449 (2013).
91. X. Ma, C.-H. Liu, G. Chang, and A. Galvanauskas, "Angular-momentum coupled optical waves in chirally-coupled-core fibers," Opt. Express **19**, 26515 (2011).
92. J. M. Fini, J. W. Nicholson, R. S. Windeler, E. M. Monberg, L. Meng, B. Mangan, A. Desantolo, and F. V DiMarcello, "Low-loss hollow-core fibers with improved single-modedness.," Opt. Express **21**, 6233–42 (2013).
93. J. M. Fini, B. Mangan, L. Meng, E. M. Monberg, J. W. Nicholson, and R. S. Windeler, "37-Cell Hollow-Core-Fiber Designs With Improved Single-Modedness," in *Cleo: 2014* (OSA, 2014), p. SM1N.2.
94. T. Murao, K. Saitoh, and M. Koshiba, "Multiple resonant coupling mechanism for suppression of higher-order modes in all-solid photonic bandgap fibers with heterostructured cladding.," Opt. Express **19**, 1713–27 (2011).
95. A. Baz, L. Bigot, G. Bouwmans, and Y. Quiquempois, "Single-mode, large mode area, solid-core photonic bandgap fiber with hetero-structured cladding," J. Light. Technol. **31**, 830–835 (2013).
96. A. W. Snyder and J. D. Love, *Optical Waveguide Theory* (Chaptman and Hall Ltd, 1983).
97. J. W. Nicholson, A. D. Yablon, J. M. Fini, and M. D. Mermelstein, "Measuring the modal content of large-mode-area fibers," IEEE J. Sel. Top. Quantum Electron. **15**, 61–70 (2009).
98. D. N. Schimpf, R. a Barankov, and S. Ramachandran, "Cross-correlated (C2) imaging of fiber and waveguide modes.," Opt. Express **19**, 13008–13019 (2011).
99. F. Kong, G. Gu, T. W. Hawkins, J. Parsons, M. Jones, C. Dunn, M. T. Kalichevsky-Dong, S. P. Palese, E. Cheung, and L. Dong, "Quantitative mode quality characterization of fibers with extremely large mode areas by matched white-light interferometry," Opt. Express **22**, 14657 (2014).

100. R. Royon, J. Lhermite, L. Sarger, and E. Cormier, "High power, continuous-wave ytterbium-doped fiber laser tunable from 976 to 1120 nm," Opt. Express **21**, 13818 (2013).
101. A. Tünnermann, T. Schreiber, and J. Limpert, "Fiber lasers and amplifiers: an ultrafast performance evolution.," Appl. Opt. **49**, F71–F78 (2010).
102. R. Steinborn, A. Koglbauer, P. Bachor, T. Diehl, D. Kolbe, M. Stappel, and J. Walz, "A continuous wave 10 W cryogenic fiber amplifier at 1015 nm and frequency quadrupling to 254 nm.," Opt. Express **21**, 22693–8 (2013).
103. J. Nilsson, J. D. Minelly, R. Paschotta, a C. Tropper, and D. C. Hanna, "Ring-doped cladding-pumped single-mode three-level fiber laser.," Opt. Lett. **23**, 355–357 (1998).
104. H. Xiao, P. Zhou, X. L. Wang, S. F. Guo, and X. J. Xu, "High power 1018 nm monolithic Yb 3+ -doped fiber laser and amplifier," Laser Phys. Lett. **9**, 748–753 (2012).
105. H. Xiao, P. Zhou, X. L. Wang, X. J. Xu, and Z. J. Liu, "High power 1018 nm ytterbium doped fiber laser with an output power of 309 W," Laser Phys. Lett. **10**, 065102 (2013).
106. S. Suzuki, H. a McKay, X. Peng, L. Fu, and L. Dong, "Highly ytterbium-doped silica fibers with low photo-darkening.," Opt. Express **17**, 9924–9932 (2009).
107. A. V Kir'yanov and Y. O. Barmenkov, "Cooperative luminescence and absorption in Ytterbium-doped silica fiber and the fiber nonlinear transmission coefficient at λ = 980 nm with a regard to the Ytterbium ion-pairs' effect: Reply.," Opt. Express **14**, 6983–6985 (2006).